The Role of the "Atmospheric Bridge" in Linking Tropical Pacific ENSO Events to Extratropical SST Anomalies

NGAR-CHEUNG LAU AND MARY JO NATH

Geophysical Fluid Dynamics Laboratory/NOAA, Princeton University, Princeton, New Jersey

(Manuscript received 31 July 1995, in final form 23 February 1996)

ABSTRACT

The role of the atmospheric circulation as a "bridge" between sea surface temperature (SST) anomalies in the tropical Pacific and those in the midlatitude northern oceans is assessed. The key processes associated with this atmospheric bridge are described using output from four independent simulations with a general circulation model subjected to month to month SST variations observed in the tropical Pacific during the 1946–1988 period and to climatological SST conditions elsewhere (the "TOGA" runs). In episodes with prominent SST anomalies in the tropical Pacific, extratropical perturbations in the simulated atmospheric temperature, humidity, and wind fields induce changes in the latent and sensible heat fluxes across the air–sea interface of the midlatitude oceans. These anomalous fluxes in turn lead to extratropical SST changes.

The relevance of the atmospheric bridge mechanism is evaluated by driving a motionless, 50-m deep oceanic mixed layer model at individual grid points with the local surface fluxes generated in the TOGA runs. The negative feedback of the mixed layer temperature anomalies on the imposed flux forcing is taken into account by introducing a linear damping term with a 5-month dissipative time scale. This simple system reproduces the basic spatial and temporal characteristics of the observed SST variability in the North Pacific and western North Atlantic.

The two-way air–sea feedbacks associated with the atmospheric bridge are investigated by performing four additional 43-year runs of a modified version of the TOGA Experiment. These new "TOGA-ML" runs predict the ocean temperature outside the tropical Pacific by allowing the atmosphere to interact fully with the same mixed layer model mentioned above. The results support the notion that midlatitude ocean–atmosphere interaction can be modeled as a first-order Markov process, in which the red-noise response of mixed layer temperature is driven by white-noise atmospheric forcing in the presence of linear damping.

The amplitude of near-surface atmospheric anomalies appearing in the TOGA-ML runs is higher than that in the TOGA runs. This finding implies that, in the TOGA-ML scenario, the midlatitude oceanic responses to atmospheric driving could exert positive feedbacks on the atmosphere, thereby reinforcing the air–sea coupling. The enhanced atmosphere–ocean interactions operating in TOGA-ML prolong the duration of persistent meteorological episodes in that experiment. A comprehensive survey is conducted of the persistence characteristics simulated in TOGA, TOGA-ML, and several other experiments subjected to prescribed SST forcing at various sites. Model scenarios in which observed tropical Pacific SST anomalies act in conjunction with SST perturbations in midlatitudes (either prescribed or predicted) are seen to produce the highest frequency of persistent events.

1. Introduction

It is well known from various empirical studies that prominent sea surface temperature (SST) signals associated with El Niño–Southern Oscillation (ENSO) events are present not only within the tropical Pacific, but also in several remote sites in the World Ocean. Of particular interest to the present study are the SST changes in the extratropical northern oceans during such ENSO episodes. Weare et al. (1976) noted that above-normal SST conditions in the equatorial Pacific are accompanied by anomalously cold waters in the central North Pacific, warm waters off the western North American coasts, and vice versa. Global analyses by Hsiung and Newell (1983) and Pan and Oort (1990) further indicate that ENSO variability in the tropical Pacific is correlated with a dipolelike structure in the SST anomaly field in the western North Atlantic. The physical origin of these relationships between SST changes at distant sites is clearly an important issue in our ongoing quest for an understanding of the global ocean–atmosphere variability on interannual timescales.

The connection between SST variability in tropical and midlatitude sites was investigated by Alexander (1990, 1992a,b) and Luksch and von Storch (1992), who have subjected various models of the extratropical ocean to driving by atmospheric anomalies related to ENSO. The midlatitude oceanic response obtained in these studies is consistent with the observed relation-

Corresponding author address: Dr. Ngar-Cheung Lau, GFDL/NOAA, Princeton University, P.O. Box 308, Princeton, NJ 08542.

ship between ENSO events and the SST field in the North Pacific. Analogous experiments by Miller et al. (1994) using an ocean general circulation model demonstrate that extratropical oceanic variability on interdecadal timescales, such as that associated with the pronounced shift in the conditions of the North Pacific during 1976–1977, is also related to fluctuations in the atmospheric driving.

In a more recent study by Lau and Nath (1994, hereafter referred to as LN94), the observed month to month SST variations during the 1946–1988 period were inserted in the lower boundary condition of a 15-wavenumber, nine-layer atmospheric general circulation model (GCM) developed at the Geophysical Fluid Dynamics Laboratory. Separate model runs were conducted by applying the temporally varying SST forcing in each of three different domains: near-global ocean, tropical Pacific only, and extratropical North Pacific only. The surface temperatures at all maritime grid points situated outside the domain of variable forcing for a given run were fixed at their climatological seasonal values. By diagnosing the output of four independent integrations initiated from different atmospheric conditions and subjected to varying forcing in the tropical Pacific only [referred to as TOGA (Tropical Ocean and Global Atmosphere) runs by LN94], it was reported that the imposed tropical SST variations are particularly effective in generating a wavelike atmospheric response spanning over the North Pacific–North American sector during winter. The prominent role of tropical Pacific SST anomalies in forcing this atmospheric pattern is also evident in other GCM experiments conducted by Graham et al. (1994) and Ferranti et al. (1994). It was noted in LN94 that the sea level wind, temperature, and humidity perturbations associated with the characteristic wave train lead to well-defined anomalies in the sensible and latent heat fluxes at the surface of the North Pacific and North Atlantic Oceans. The spatial pattern of the implied SST tendency driven by these model-generated surface fluxes is in good agreement with that of the observed extratropical SST changes accompanying ENSO.

The modeling studies cited above indicate that the atmosphere serves as a crucial link between interannual SST fluctuations in different parts of the World Ocean. This "atmospheric bridge" owes its existence primarily to SST forcing in the tropical Pacific, but in turn acts as a driving mechanism for oceanic variability in higher latitudes. The primary objective of the present study is to further investigate different facets of the atmospheric bridge mechanism through more detailed diagnoses of the existing TOGA runs, as well as through the examination of additional model experiments incorporating various degrees of interaction between the atmosphere and ocean.

The observed relationships between SST anomalies in the tropical Pacific and in the northern extratropical oceans are reviewed briefly in section 2. The midlatitude circulation anomalies forced by SST changes in the tropical Pacific, and the roles of such atmospheric variations in altering various forms of heat exchange across the local air–sea interface, are documented in section 3 using output from the TOGA experiment. In section 4, the influences of the surface heat flux anomalies upon the extratropical oceans are determined from the responses of a simple mixed layer model to different types of atmospheric driving. The spectral behavior of the surface flux forcing and SST response is examined in section 5. The impact of the midlatitude SST variations on the overlying atmosphere is explored in section 6 by allowing two-way feedbacks between changes in the mixed layer and the model atmosphere.

2. An index of ENSO and its covariability with SST in the northern oceans

The basic premise of LN94 and the present study is that the variability of the extratropical atmosphere–ocean system is linked to SST anomalies in the tropical Pacific. It is therefore useful at the outset to develop an index of the principal mode of SST perturbations in the latter region. The spatial and temporal patterns associated with this mode are obtained by conducting a principal component (PC) analysis of the observed SST field in the tropical Pacific between 20°S and 20°N. The database for this analysis consists of northern winter means (i.e., averages over December, January, and February) for the 1946–1988 period. These ship measurements of SST were originally assembled in the Comprehensive Ocean–Atmosphere Data Set (COADS, see Woodruff et al. 1987) and were subsequently analyzed on a global ocean grid using an objective interpolation scheme (see Pan and Oort 1990).

The leading PC of the tropical Pacific SST field explains 52% of the domain-integrated variance. The time series of the temporal coefficients associated with this leading mode is displayed in Fig. 1a. The values shown here are obtained by normalizing the coefficients for individual winters by one standard deviation as computed on the basis of the entire time series. The spatial pattern for the same mode may be depicted by the distribution of the regression coefficients of the SST anomalies at individual grid points versus the time series in Fig. 1a. This pattern, shown in Fig. 1b, indicates the polarity and amplitude (in °C) of the local SST anomaly for each standard deviation of the temporal coefficients above or below zero. The chart in Fig. 1b is reminiscent of the typical SST anomaly pattern during the mature phase of ENSO (e.g., Rasmusson and Carpenter 1982). Particularly noteworthy is the elongated equatorial extremum extending from near the date line to the Peru–Ecuador coast.

The temporal coefficients in Fig. 1a clearly depict the prominent warm and cold ENSO episodes. Also evident in this time series is the prolonged period of mostly above-normal tropical Pacific SST from 1976–

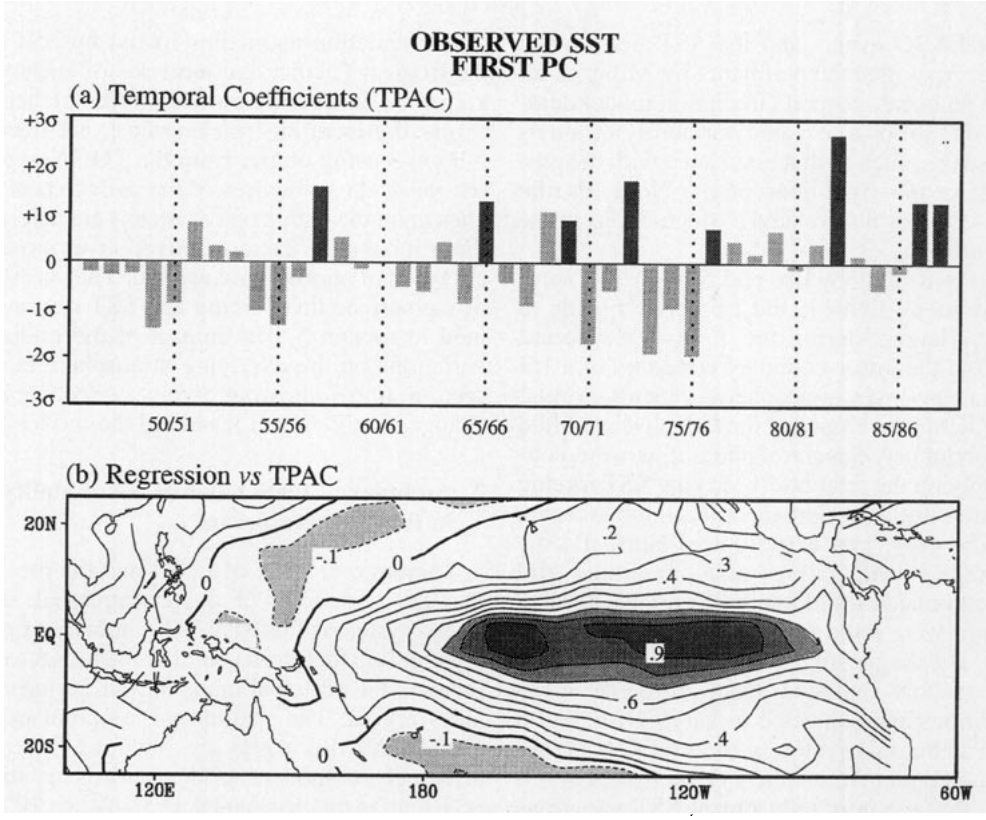

FIG. 1. (a) Time series of temporal coefficients (referred to as TPAC in the text) and (b) spatial pattern associated with the first principal component of the observed SST field in the tropical Pacific during the northern winter. The temporal coefficients in individual seasons are normalized by the standard deviation for the entire 42-winter record. Prominent warm El Niño winters are indicated as black columns. The spatial pattern shows the distribution of the regression coefficients of the observed SST data at individual grid points versus TPAC. Contour interval: 0.1°C.

1977 through 1988. We shall henceforth use the time series in Fig. 1a to delineate the covariability of selected extratropical fields with ENSO-related SST fluctuations in the tropical Pacific. Ample use will be made of regression charts of pertinent variables versus this reference time series (hereafter referred to as the "TPAC" time series). We note that the peak values in the equatorial extremum in Fig. 1b are ~1°C per standard deviation of the temporal coefficients. The values appearing in the regression charts to be shown in this paper may be viewed as the typical amplitude of the variable being examined for ~1°C of warming in the equatorial Pacific. The correlation coefficients between the TPAC time series and other commonly used indexes of ENSO, such as the seasonal SST anomaly averaged over the NINO3 (5°S–5°N, 90°–150°W) and NINO4 (5°S–5°N, 150°W–160°E) regions, are as high as 96% and 93%, respectively. Hence the gross characteristics of these regression charts should not be sensitive to our particular choice of TPAC as the reference time series.

The relationship between tropical ENSO events and extratropical SST changes is illustrated in Fig. 2, which shows the regression coefficients of observed winter-mean SST variations at individual grid points in the North Pacific and western North Atlantic versus the reference time series in Fig. 1a. The corresponding distribution of correlation coefficients will be presented later in Fig. 7a. It is evident from the regression chart in Fig. 2 that warm ENSO events are coincident with cold SST anomalies in the central North Pacific, and warm anomalies in the western subtropical Pacific and along the west coast of North America. A dipole-like pattern is also discernible in the western North Atlantic. Much of the results presented in the following sections are devoted to the understanding of various processes contributing to the pattern in Fig. 2.

3. Surface fluxes associated with extratropical atmospheric anomalies simulated in TOGA

The TOGA experiment, in which time-varying SST conditions are prescribed in the tropical Pacific only (see LN94 for details), is particularly suited for assessing the impact of tropical ENSO on the extratropical atmospheric circulation. Here we examine a variety

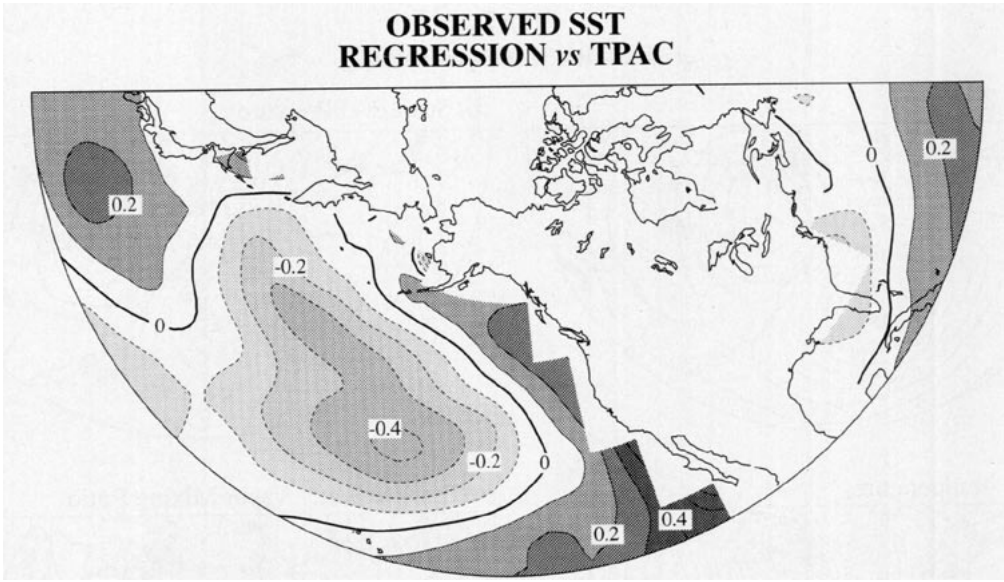

FIG. 2. Distribution of regression coefficients of observed wintertime SST data at individual grid points in the North Pacific and western North Atlantic versus the reference TPAC time series in Fig. 1a. Contour interval: 0.1°C. For this and other polar stereographic charts displayed in the present paper, the plotting domain extends from 20° to 90°N, 130°E to 50°W.

of model fields generated in TOGA that have direct bearing on different forms of air–sea exchange. The regression patterns of the winter-mean (a) 515-mb height and (b) sea level pressure, as well as variations at the lowest model level of (c) temperature, (d) water vapor mixing ratio, (e) wind speed, and (f) horizontal wind vector versus the TPAC time series, are presented in Fig. 3. The lowest model level is situated at an altitude of about 85 m above sea level. All regressions are performed using model data that have been averaged over the four individual realizations of the TOGA experiments (i.e., the "four-run ensemble averages" referred to in LN94).

The charts for 515-mb height and sea level pressure (Figs. 3a–b) are indicative of an equivalent barotropic wavelike response in the North Pacific–North American sector. The near-surface circulation pattern (Fig. 3f) is characterized by an anomalous cyclonic cell over the Pacific and prevalent southwesterlies over the western Atlantic. The pattern of the changes in wind speed (Fig. 3e) is determined by the alignment of the anomalous wind vector with the climatological circulation. For the region poleward of ~30°N, where climatological westerlies prevail, the wind speed is increased when the anomalous flow is directed eastward, and vice versa. The opposite situation applies in the climatological easterly regime over the subtropical oceans. The changes in near-surface temperature and humidity (Figs. 3c–d) exhibit a notable relationship with the advection of temperature and moisture by the local anomalous circulation. Anomalous wind vectors (see Fig. 3f) originating from relatively warm and moist regions are coincident with above normal temperature and mixing ratio, and vice versa. As was noted in LN94, the amplitude of the simulated 515-mb anomalies is weaker than observed by a factor of 2–3. We therefore expect that the responses of other model variables displayed in Fig. 3 are also underestimated.

The regression charts of (a) latent heat flux, (b) sensible heat flux, (c) radiative flux, and (d) sum of latent, sensible, and radiative fluxes versus the TPAC time series are displayed in Fig. 4. The winter means of the four-run ensemble averages of the TOGA output are used in this computation. For all surface fluxes, we have adopted the sign convention that positive fluxes are directed from the atmosphere to the ocean (thus leading to positive SST tendencies). The patterns for the latent and sensible heat fluxes (Figs. 4a,b) are qualitatively similar. For a given location, the amplitude of the latent heat fluxes is higher than that of the sensible heat fluxes in subtropical latitudes, whereas the sensible fluxes are stronger than latent fluxes poleward of ~50°N. During warm ENSO events, the model generates negative anomalies in latent and sensible fluxes (oceanic cooling) over the central North Pacific and the coastal Atlantic waters off the northeastern seaboard of North America, and positive flux anomalies (oceanic warming) over the Gulf of Alaska, subtropical Atlantic, and the southwestern corner of the North Pacific.

The GCM computes the latent and sensible heat fluxes by using the bulk aerodynamic law (see formulas given in section 4a), which relates the fluxes to the product of the local surface wind speed and

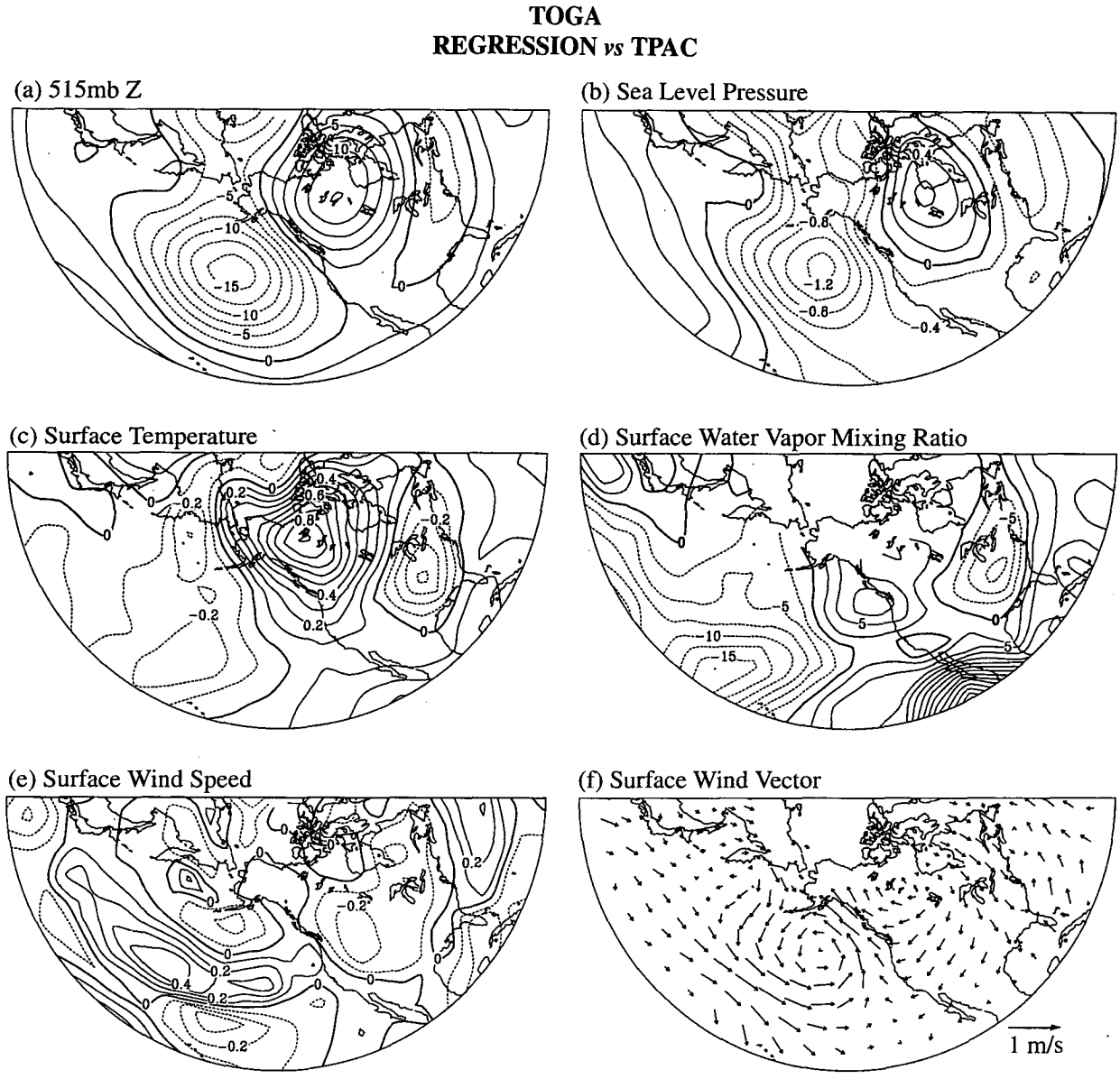

FIG. 3. Distribution of regression coefficients of four-run ensemble average wintertime data from the TOGA experiment versus the reference TPAC time series in Fig. 1a for (a) 515-mb height, contour interval: 2.5 m; (b) sea level pressure, contour interval: 0.2 mb; (c) surface air temperature, contour interval: 0.1°C; (d) surface water vapor mixing ratio, contour interval: 2.5×10^{-5}; (e) surface wind speed, contour interval: 0.1 m s^{-1}; and (f) surface wind vector (see scale at lower right).

air to sea difference in temperature or mixing ratio. Since the SST conditions at all oceanic grid points outside of the tropical Pacific have been fixed at their climatological values in the TOGA experiment, anomalies in the air to sea difference in the extratropics are determined solely by fluctuations in the near-surface atmospheric temperature and mixing ratio. The relationships between the fluxes and the surface atmospheric variables are discernible from the pertinent regression charts in Figs. 3 and 4. The patterns in Figs. 4a,b bear a strong resemblance to those of the temperature and humidity fields (Figs. 3c,d), with warm moist air masses being collocated with positive heat fluxes, and vice versa. Additional computations (not shown) also indicate that the seasonal anomalies of surface heat fluxes are more strongly correlated with the local changes in air temperature or humidity than with variations in the local wind speed. Hence the air–sea exchange of latent and sensible heat is primarily governed by fluctuations in temperature and humidity in the boundary layer of the model atmosphere,

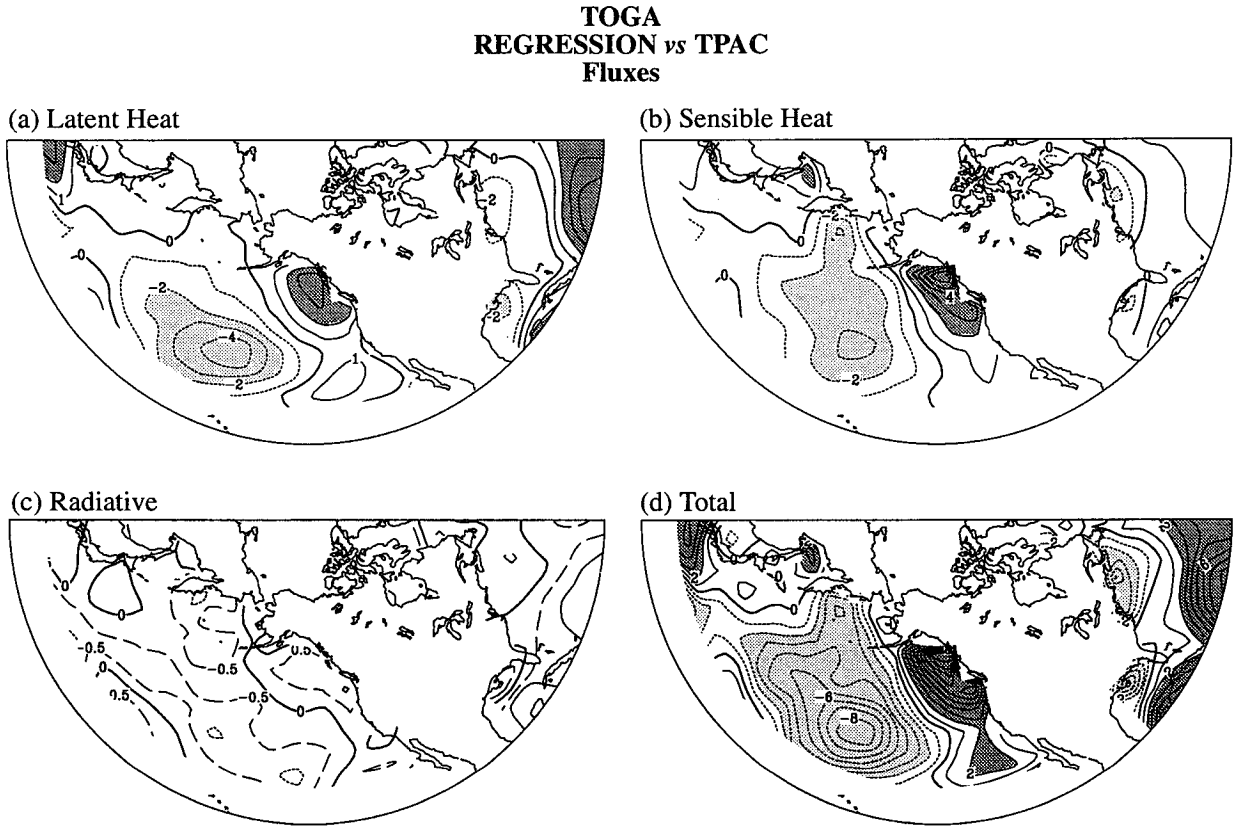

FIG. 4. As in Fig. 3 but based on TOGA data for (a) latent heat flux, (b) sensible heat flux, (c) radiative flux, and (d) sum of latent heat, sensible heat, and radiative fluxes. Contour interval for (a), (b), and (d): 1 W m^{-2}. Contour interval for (c): 0.5 W m^{-2}.

whereas variations in the surface wind speed play a secondary role.

The spatial relationships between the latent and sensible heat fluxes and the near-surface wind, temperature, and humidity fields, as inferred from the TOGA experiment, are similar to the observational results reported by Cayan (1992a), who presented correlation charts of these fields versus an index of the Pacific/North American pattern. However, due to underestimation of the wind, temperature, and humidity anomalies in the model atmosphere, the amplitude of the simulated heat fluxes are notably weaker than that reported in Cayan's study.

The amplitude of the radiative flux anomalies (Fig. 4c) is ~20%–30% of the corresponding values for the latent and sensible heat fluxes. Variations in the extratropical radiative forcing are mainly a consequence of the perturbations of cloud cover accompanying spatial displacements in the midlatitude rainbelts, which are in turn related to changes in the large-scale atmospheric circulation (and the transient disturbances embedded therein) as described in Fig. 3.

The sum of the simulated anomalous fluxes (Fig. 4d) is in good agreement with the regression chart for the observed SST anomaly (Fig. 2), thus indicating that the model-generated extratropical response to tropical Pacific SST changes could in turn drive realistic SST changes in the North Pacific and North Atlantic. The time scale required for the simulated atmospheric driving to generate extratropical SST anomalies with the observed intensity, as estimated by dividing the regression coefficients for SST (Fig. 2) by the corresponding values for fluxes (Fig. 4d) at the same sites, is approximately 4 months for an oceanic mixed layer with an assumed depth of 50 m.

Cayan (1992b) has documented the dominant modes of variability in extratropical latent and sensible heat fluxes based on ship observations. His results also indicate that these anomalous heat flux patterns are strongly correlated with observed month to month changes in the SST field, especially during the cool season. These observational findings support the notion that the midlatitude SST variations are primarily driven by the surface fluxes.

4. The atmospheric bridge in action—Experimentation with an oceanic mixed layer model

a. Model scenarios

The inferences on the atmospheric bridge mechanism, as drawn from the model diagnosis in the pre-

ceding section, are tested here by examining the interaction of a simple mixed layer model of the extratropical ocean with the overlying atmosphere. The mixed layer at each maritime grid point is represented by a column of motionless water with a fixed depth of 50 m. The fluctuations of the mixed layer temperature at a certain site are determined solely by the fluxes across the air–sea interface at the same site. No direct interaction is allowed between mixed layers at adjacent grid points. Three model scenarios are used to study the impact of the atmospheric bridge upon the mixed layer temperature. These experiments incorporate increasing degrees of coupling between the mixed layer and the atmosphere and are described as follows.

1) Experiment A

The mixed layer responds passively to the surface fluxes simulated in the TOGA experiment (see left panel of Fig. 5). Perturbations in the mixed layer temperature have no effect on the imposed fluxes and the atmosphere. The anomalous temperature of the mixed layer T'_o at individual grid points is given by

$$\frac{\partial}{\partial t} T'_o = \frac{F'_{\mathrm{TOGA}}}{\rho_0 C_{p0} H}, \qquad (1)$$

where the prime indicates anomalies; the subscript o indicates oceanic quantities; ρ_0 is the density of water; C_{p0} is the specific heat of water; $H = 50$ m is the constant depth of the mixed layer column; and F'_{TOGA} is the sum of anomalous latent, sensible, and radiative fluxes generated in the TOGA experiment. Monthly mean values of the four-run ensemble average of F'_{TOGA} are used as the forcing function for the above equation. The solution for T'_o is obtained by integrating this equation forward with a one-month time step and assuming that $T'_o = 0$ initially.

2) Experiment B

A framework similar to that of experiment A is adopted here, except that feedbacks between the fluctuations in T_o and F_{TOGA} are incorporated in a simple form (see middle panel of Fig. 5). The nature of these feedbacks may be illustrated by the formulas used in our GCM for computing latent heat (F_{lh}), sensible heat (F_{sh}), and outgoing longwave fluxes (F_{lw}); that is,

$$F_{\mathrm{lh}} = -\rho_a L C_D V_a (q_s - q_a),$$

$$F_{\mathrm{sh}} = -\rho_a C_{pa} C_D V_a (T_o - T_a),$$

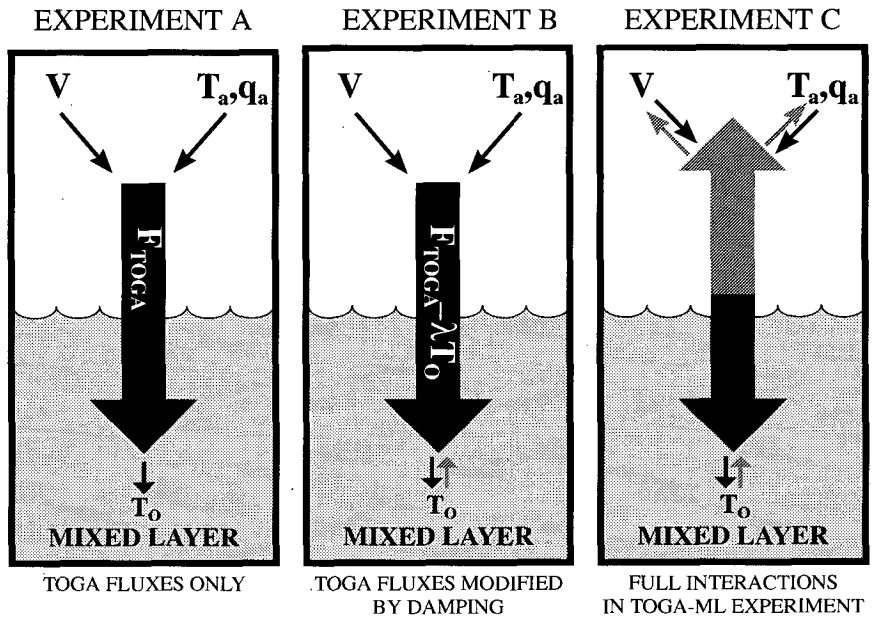

FIG. 5. Schematic diagram illustrating various degrees of air–sea coupling in experiments A (with mixed layer responding passively to surface fluxes generated in TOGA, left panel), B (with the responses to TOGA-generated surface fluxes being modulated by linear damping, middle panel), and C (the TOGA-ML runs, with full two-way interactions between the model atmosphere and mixed layer, right panel). The symbols V, T, and q denote wind speed, temperature, and water vapor mixing ratio, respectively. The subscripts a and o denote atmospheric and oceanic quantities, respectively. Black arrows correspond to pathways by which the atmosphere influences the mixed layer. Faint arrows correspond to pathways by which the mixed layer influences the atmosphere or the imposed fluxes.

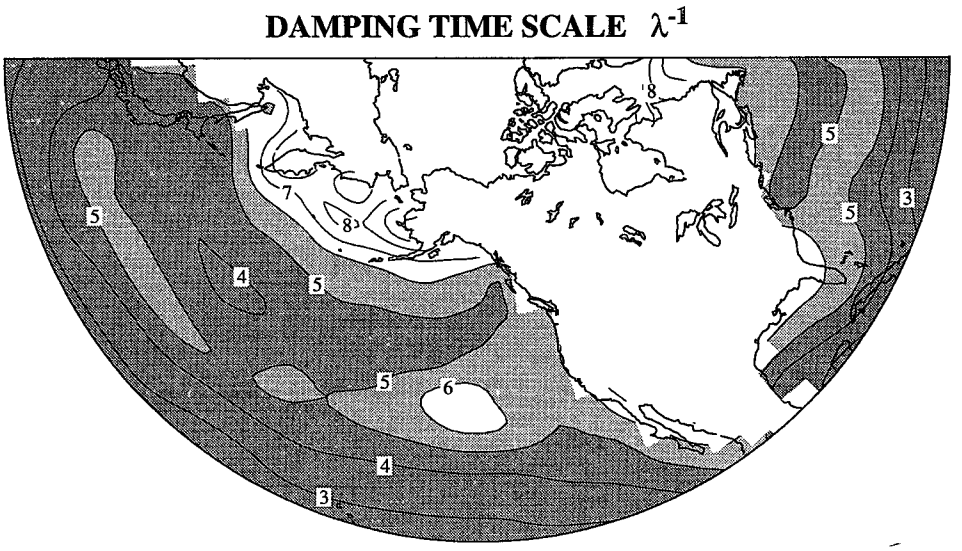

FIG. 6. Distribution of the damping time scale [λ^{-1} in Eq. (2)] for a 50-m deep mixed layer, as estimated using wintertime climatological data from the TOGA runs. Contour interval: 1 month.

and

$$F_{\text{lw}} = -\sigma_{\text{SB}} T_o^4,$$

where the subscript a refers to atmospheric quantities; ρ_a and C_{pa} are the density and specific heat of air, respectively; C_D is the drag coefficient, set to a constant value of 10^{-3}; V_a is the surface wind speed; T_a, q_a are the temperature and water vapor mixing ratio at the lowest atmospheric level; q_s is the saturation mixing ratio at T_o; L is the latent heat of vaporization; and σ_{SB} is the Stefan–Boltzmann constant. Assuming that the changes in T_o have no effect on the atmospheric quantities T_a, q_a, and V_a, the anomalous form of the above formulas due to perturbations in T_o can be written as

$$F'_{\text{lh}} = -\rho_a L C_D V_a \left(\frac{dq_s}{dT}\right) T'_o$$

$$F'_{\text{sh}} = -\rho_a C_{pa} C_D V_a T'_o$$

$$F'_{\text{lw}} = -4\sigma_{\text{SB}} T_o^3 T'_o,$$

where q'_s has been expressed as $(dq_s/dT)T'_o$. The feedback effect of T'_o on the imposed surface fluxes thus takes the form of a linear damping term $-\lambda T'_o$, where

$$\lambda = \frac{\left(\rho_a L C_D V_a \dfrac{dq_s}{dT} + \rho_a C_{pa} C_D V_a + 4\sigma_{\text{SB}} T_o^3\right)}{\rho_0 C_{p0} H}, \quad (2)$$

and Eq. (1) can be modified as

$$\frac{\partial}{\partial t} T'_o = \frac{F'_{\text{TOGA}}}{\rho_0 C_{p0} H} - \lambda T'_o. \quad (3)$$

The dissipative effect of T'_o on F'_{lh} and F'_{sh} may also be illustrated as follows. Suppose we have initially $T_o > T_a$ and $q_s > q_a$, then $F_{\text{lh}} < 0$ and $F_{\text{sh}} < 0$, which would result in negative tendencies in T_o and q_s. If T_a and q_a are fixed, T_o and q_s would gradually approach T_a and q_a, respectively, so that F_{lh} and F_{sh} would diminish with time.

The damping coefficient λ can be estimated by substituting in Eq. (2) the climatological northern wintertime values of V_a, T_o, and dq_s/dT for the TOGA experiment. The spatial distribution of λ^{-1} (which is a measure of the damping timescale) at individual grid points is shown in Fig. 6. In accordance with Eq. (2), the spatial pattern of λ^{-1} is primarily governed by variations of dq_s/dT (which increases with increasing temperature toward the subtropics) and V_a (which attains maximum strength in central Pacific and western Atlantic at ~40°N). The characteristic damping time scale is approximately 4–5 months in the midlatitude North Pacific and North Atlantic. Henceforth we shall present the solution for T'_o in Eq. (3) by using a constant value of $\lambda^{-1} = 5$ mo for all maritime grid points in the northern oceans. Supplementary calculations with λ^{-1} ranging from 2 to 10 months (not shown) confirm that the qualitative nature of our results is not sensitive to our choice. Separate plots of λ^{-1} corresponding to the latent heat, sensible heat, and radiative components (not shown) indicate that the damping due to latent heat fluxes is more important than sensible heat and radiative effects.

Frankignoul and Reynolds (1983) have estimated the damping time scale by spectral filtering of observational data and reported a value of 2.7 months for λ^{-1} for the North Pacific. In comparing this finding with our result, it should be borne in mind that the two estimates are based on rather different analysis approaches, treatments of seasonality, and assumptions of the mixed layer depth.

3) EXPERIMENT C

A crucial assumption made in the previous two experiments is that variations in T_o have no impact on the atmospheric quantities T_a, q_a, and V_a. This simplification enables us to compute T_o using the TOGA output in an "off-line" fashion, that is, after the completion of the entire suite of 43-year TOGA runs, all of which having been conducted without taking the T_o variations into account.

To allow for a two-way air–sea coupling, a modified version of the TOGA experiment is conducted (see right panel of Fig. 5). The same 15-wavenumber, nine-level atmospheric GCM used in LN94 (see also Gordon and Stern 1982) is subjected to month to month SST anomalies observed in the tropical Pacific (25°S–25°N) during 1946–1988. The physical processes treated in the model include a full hydrological cycle, radiative transfer, sea ice formation, and soil moisture variations. Realistic orography and ocean–continent contrast are represented at the lower boundary. The new experiment (hereafter referred to as TOGA-ML, with "ML" denoting the use of a mixed layer) differs from the previous TOGA runs in the treatment of the lower boundary condition at maritime grid points outside of the tropical Pacific. Instead of prescribing the climatological SST conditions at these locations, the TOGA-ML experiment computes the T_o variations once per day in the course of the GCM integration. The same 50-m static mixed layer described earlier is used to obtain T_o. In this scenario, variability in the heat and radiative fluxes at the air–sea interface not only leads to fluctuations in T_o, but also simultaneously to changes in the model atmosphere (in particular, T_a, q_a, and V_a). As in TOGA, altogether four independent 43-year integrations have been performed, with each run being initiated from a different set of atmospheric conditions.

To facilitate a smooth transition from the prescribed SST observations in the tropical Pacific to the predicted T_o variations farther north and south, two buffer zones are incorporated along the rows of grid points near 25°N and 25°S in the Pacific. At any given time in the integration, the temperature in these zones is taken to be the average of the local SST observation and the predicted T_o at that time.

To ensure that the long-term-averaged seasonal cycle of T_o resembles that of the observed climate, the flux correction procedure developed by Manabe and Stouffer (1988) has been applied to all maritime grid points outside of the tropical Pacific. The corrections over the wintertime extratropical North Pacific and North Atlantic typically amount to 10%–20% of the local climatological mean values for the total surface fluxes. We emphasize here that these flux corrections are first computed on the basis of the seasonal climatology of the specific GCM used here. For a given phase of the seasonal cycle and a given grid point, the same correction is then applied to the mixed layer throughout the experiment, regardless of the strength and polarity of the SST anomalies generated in the course of the model run. This procedure would therefore minimize the impact of the correction on the relationship between the anomalous SST and flux behavior being examined here.

An analogous set of three experiments have earlier been performed by Alexander (1992a), who interpreted the modes of interaction in experiments A, B, and C as "one-way forced," "partially coupled," and "fully coupled," respectively. The present study complements Alexander's work by reexamining the atmospheric bridge mechanism through the detailed analysis of a more extended suite of model integrations.

b. Response patterns of T_o

The response of T_o to forcing by the atmospheric bridge, as computed using the three methods described in the previous subsection, is compared with the corresponding observations in Fig. 7. The left panels of this diagram show the spatial distributions of the temporal correlation coefficient between the TPAC time series (see Fig. 1a) and T_o at individual grid points. The corresponding charts for correlation between TPAC and tendency of T_o are displayed in the right panels. These tendency charts are intended for discerning the existence, if any, of quadrature relationships between ENSO-related forcing and the T_o response. The patterns for the observed SST data are presented in the top row, followed by the results based on experiments A, B, and C in the second, third, and fourth rows, respectively. All model fields are computed using four-run ensemble averages. The patterns in the left column are derived from SST or T_o data averaged over the winter months of December, January, and February. The temperature tendency field used in constructing the patterns in the right column is defined as the difference between the data averaged over October and November from those averaged over March and April. This definition is admittedly only a crude measure of the SST tendency. It is, however, worth noting that results based on slight variations in the definition of this tendency (not shown) lead to essentially the same conclusions.

Use of the normalized correlation coefficients in Fig. 7, instead of the regression coefficients displayed in previous figures, facilitates the comparison of the covariability of TPAC with various fields that have different physical units [e.g., SST (in °C) and SST tendency (in °C mo^{-1})] and different characteristic amplitudes (e.g., observed SST anomalies are stronger than simulated anomalies; see Figs. 2 and 8).

The correlation pattern based on observed SST data (Fig. 7a) resembles the corresponding regression pattern shown earlier in Fig. 2. Comparison between Figs. 7a and 7b indicates that the level of correlation between

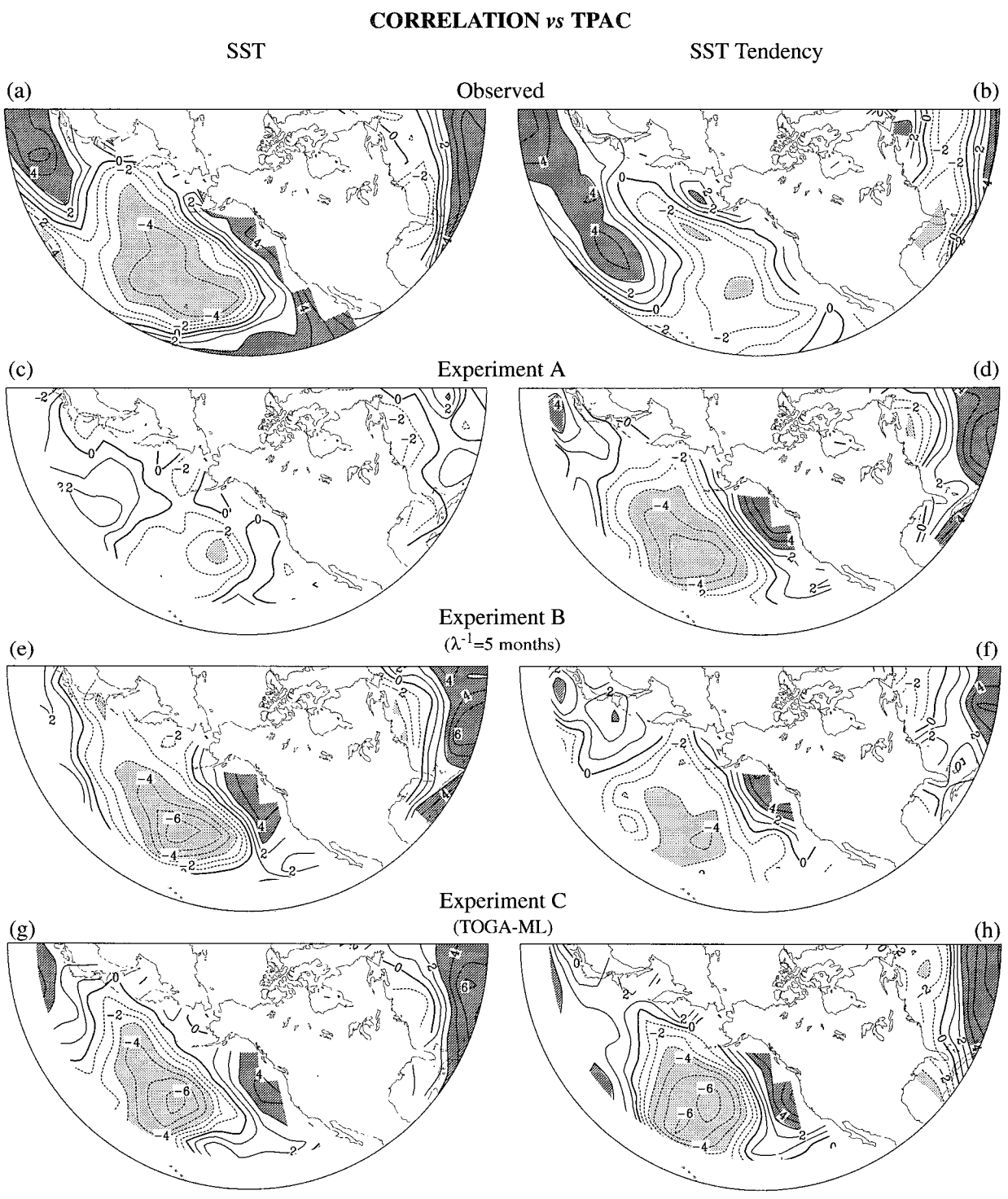

FIG. 7. Distribution of temporal correlation coefficients of the reference TPAC time series in Fig. 1a versus winter-mean (left panels) and tendency (right panels) of SST or mixed layer temperature at individual grid points, as computed using data from observations (first row) and output from experiments A (second row), B (third row), and C (fourth row). Contour interval: 1×10^{-1}. The winter-mean values correspond to averages over December, January, and February. The tendency values are obtained by subtracting the March–April average from the October–November average.

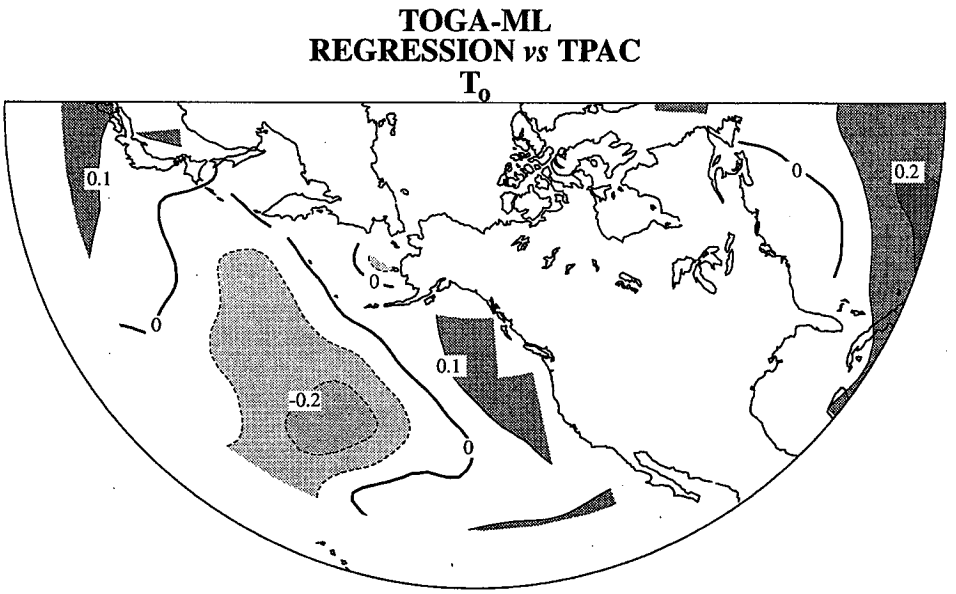

FIG. 8. As in Fig. 2, but based on four-run ensemble averaged data for mixed layer temperature produced in the TOGA-ML experiment.

TPAC and observed SST in the northern oceans is generally higher than that between TPAC and observed SST tendency.

For experiment A, TPAC exhibits strong correlations with the tendency of T_o (Fig. 7d), while the correlations with T_o itself (Fig. 7c) are much weaker. This finding is consistent with the form of Eq. (1), which states that the extratropical surface fluxes accompanying SST fluctuations in TPAC are in quadrature with T_o in midlatitudes. Indeed, comparison between Figs. 7d and 4d confirms that the distribution of T_o tendency is almost identical to that of the anomalous surface flux pattern accompanying ENSO.

The addition of the damping term in experiment B yields a pattern for T_o (Fig. 7e) with higher correlation values than those in the corresponding pattern for T_o tendency (Fig. 7f), in agreement with the observations (Figs. 7a,b). The more realistic results in experiment B can be understood in light of Eq. (3). For interannual variations of T_o, the tendency term on the lhs of this equation is much smaller than the damping term $-\lambda T_o'$, since λ^{-1} is set to equal to 5 months (see Fig. 6). For ENSO timescales, the damping term is essentially balanced by the flux term, that is,

$$\frac{F'_{\mathrm{TOGA}}}{\rho_0 C_{p0} H} \approx \lambda T_o',$$

with T_o' being in phase with F'_{TOGA} (and hence with TPAC).

The correlation chart for T_o based on output from the TOGA-ML runs in experiment C (Figs. 7g) is similar to its counterpart for experiment B (Fig. 7e) with regards to both correlation strength and spatial pattern. However, unlike experiments A and B, the correlation level for T_o (Fig. 7g) produced by TOGA-ML is comparable to that for its tendency (Fig. 7h). One of the factors contributing to the latter result is the potential role of the atmospheric response to T_o fluctuations (a process not considered in experiments A and B) in intensifying the surface fluxes or in lessening the damping effect, thus making possible a three-way balance among all of the terms in Eq. (3). The implications of midlatitude air–sea coupling on the atmospheric circulation is a subject for further discussion in section 6.

The *magnitude* of the T_o anomalies simulated in experiments B and C may be inferred from the distribution of regression coefficients of T_o versus the reference TPAC time series (Fig. 1a). The result based on the wintertime, four-run ensemble average of T_o from experiment C (the TOGA-ML runs) is shown in Fig. 8. The corresponding regression chart for experiment B (not shown) is similar to this pattern. Comparison between Fig. 8 and its observational counterpart (Fig. 2) indicates that the amplitude of the signals in the model result is about half of that actually observed. A major contributing factor to this discrepancy is that the simulated midlatitude atmospheric response (which in turn drives the mixed layer underneath) to SST forcing in the tropical Pacific is typically weaker than the observed response by a factor of 2–3 (e.g., see Fig. 14 of LN94).

5. Spectral characteristics of surface fluxes and T_o response

a. Theory of stochastic model

The agreement between the results from experiment B (Figs. 7e,f) and the observations (Figs. 7a,b) indicates that Eq. (3) constitutes an appropriate framework for describing the nature of ENSO-related SST variability in the extratropics. If the characteristic timescale of T_o' is much longer than that of the atmospheric driving $F'_{\text{TOGA}}/(\rho_0 C_{p0} H)$, and if F'_{TOGA} does not exhibit any strong frequency dependence (i.e., it has a "white" spectrum), Eq. (3) is equivalent to the definition of a first-order Markov process. The central role of this process in the theory of stochastic climate models has been pointed out by Hasselmann (1976). Such conceptual models have been applied by Frankignoul and Hasselmann (1977), Frankignoul and Reynolds (1983), Lemke et al. (1980), and Delworth and Manabe (1988) in analyzing the variability of SST, sea ice, and soil moisture. Treating the T_o' response as the output of a Markov process, the spectrum $S_T(\omega)$ of T_o' can be related to the (constant) spectrum S_F of $F'_{\text{TOGA}}/(\rho_0 C_{p0} H)$ as

$$S_T(\omega) = \frac{S_F}{\omega^2 + \lambda^2}, \tag{4}$$

where ω is the frequency. Equation (4) indicates that $S_T \sim S_F/\omega^2$ for $\omega \gg \lambda$, whereas S_T approaches the constant value of S_F/λ^2 for $\omega \ll \lambda$. The variance of the fluctuations in T_o hence resides mostly in the low-frequency portion of S_T (i.e., the spectrum is "red"). Another well-known property of a first-order Markov process is that the autocorrelation function $R(\tau)$ of the output T_o' can be written as

$$R(\tau) = e^{-\lambda\tau}, \tag{5}$$

where τ is the time lag. We now proceed to examine whether the midlatitude atmospheric forcing generated in the TOGA and TOGA-ML runs meet the basic assumptions for a first-order Markov process and evaluate the adequacy of the relationships expressed in Eqs. (4)–(5) in describing the spectral behavior of the output of T_o' from TOGA-ML.

b. SVD analysis

Computation of the spectra and autocorrelation functions described in the previous subsection requires continuous time series of indexes depicting the behavior of the surface flux and mixed layer temperature fields through all 12 months of the seasonal cycle. We shall devote our attention to representative indexes of surface fluxes and T_o' in the North Pacific that exhibit strong correlations with anomalous SST episodes in the tropical Pacific. The desired temporal coefficients can readily be identified using the method of singular value decomposition (SVD) analysis, as described by Bretherton et al. (1992) and Wallace et al. (1992). In the present application, the SVD analysis has been performed separately on four pairs of fields. These four analyses will be referred to as SVDa, SVDb, SVDc, and SVDd. The left input field in all four computations is the observed tropical Pacific SST between 20°S and 20°N (hereafter abbreviated as OBS.TPAC.SST). The right input fields in the four individual SVD analyses correspond to the following variables in the North Pacific between 25° and 55°N:

- observed SST (OBS.NPAC.SST), for SVDa
- total surface heat flux simulated in the TOGA experiment (TOGA.NPAC.FLUX), for SVDb
- total surface heat flux simulated in the TOGA-ML experiment (TOGA-ML.NPAC.FLUX), for SVDc
- mixed layer temperature simulated in the TOGA-ML experiment (TOGA-ML.NPAC.SST), for SVDd.

The input data for both the left and right fields are comprised of 12 monthly means for each year in the 1946–1988 period.

We shall focus our attention on the leading mode in each of the four SVD analyses, which accounts for the highest squared covariance fraction (SCF) between the left and right fields. The SCF as explained by these modes are 83%, 73%, 66%, and 69% for SVDa, SVDb, SVDc, and SVDd, respectively. Each SVD mode is associated with a time series of monthly expansion coefficients (hereafter referred to as a) for the left field, and another time series for the right field (hereafter referred to as b). The spatial structure associated with a given mode can be discerned by a pair of heterogeneous correlation charts. The chart constructed by correlating b with the gridpoint data for the left field will be referred to as C_L. The corresponding chart depicting the correlation between a and right field will be referred to as C_R. For comparison with other results in this paper, C_L and C_R have been computed using four-run ensemble averages of the seasonal means for winter only. As a measure of the degree of coupling between the left and right fields for a given SVD pair, the temporal correlation coefficient (hereafter denoted as r) between the four-run, wintertime averages of a and b for that pair has also been evaluated. The values of r as computed in this manner are 59%, 62%, 71%, and 75% for SVDa, SVDb, SVDc, and SVDd, respectively.

The patterns of C_L as determined by all four SVD computations are similar to each other, thus indicating that the four different right fields considered here are most strongly coupled to essentially the same tropical Pacific SST anomaly. The pattern for this characteristic anomaly (not shown) resembles that of the ENSO-related SST field in Fig. 1b. The pattern of C_R for SVDa, shown in Fig. 9a, confirms that warm anomalies in the equatorial Pacific are accompanied by cold anomalies in the central North Pacific and by warm anomalies off

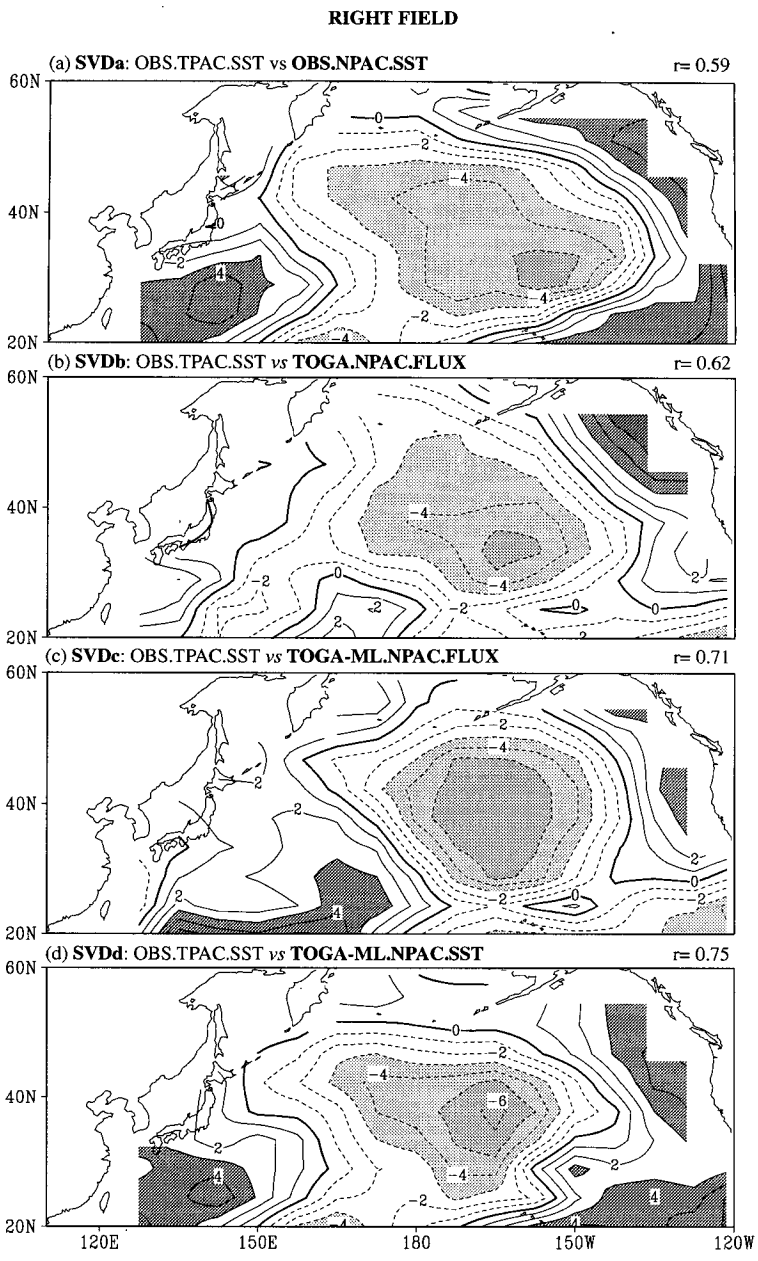

FIG. 9. Heterogeneous correlation patterns C_R of the leading modes for four individual SVD analyses, as computed by correlating the expansion coefficients of the left field with the data for the right field at individual grid points. The left field for all four SVD analyses is the observed tropical Pacific SST (OBS.TPAC.SST). The four panels shown here correspond to the distributions of C_R in the North Pacific of (a) observed SST (OBS.NPAC.SST) in SVDa, (b) TOGA-simulated total surface flux (TOGA.NPAC.FLUX) in SVDb, (c) TOGA-ML-simulated total surface flux (TOGA-ML.NPAC.FLUX) in SVDc, and (d) TOGA-ML-simulated mixed layer temperature (TOGA-ML.NPAC.SST) in SVDd. Contour interval: 1×10^{-1}. All correlation charts are based on four-run ensemble means of the seasonal averages over December, January, and February. In computing SVDb, SVDc, and SVDd, the data for the four individual TOGA or TOGA-ML runs are concatenated, so that each input time series has a total length of 4 (runs) $\times$ 43 (years) $\times$ 12 (months). All computations are based on monthly departures from the climatological seasonal cycle. The SVD analyses are performed on a matrix consisting of covariances between the left and right fields. The correlation coefficient r between the four-run, wintertime averages of the expansion coefficients for the left and right fields of a given SVD mode is displayed at the upper-right-hand corner of the pertinent pattern.

the North American coasts and in the subtropical waters south of Japan.

The patterns of C_R for SVDb and SVDc, shown in Figs. 9b,c, indicate that the surface fluxes simulated in the TOGA and TOGA-ML runs during warm ENSO episodes result in cooling of the surface waters in the central North Pacific and warming in eastern and southwestern North Pacific. The distribution of C_R for SVDd (see Fig. 9d) illustrates that the response of T_o in TOGA-ML during the warm phase of ENSO is characterized by a cold anomaly in the central North Pacific and warm anomalies farther east and west.

In much of the North Pacific, considerable similarities exist among the patterns of C_R for the four individual SVD analyses shown in Fig. 9. Inspection of the patterns of C_R obtained using the SVD technique and the corresponding regression or correlation charts based on the TPAC reference time series in Fig. 1a (i.e., compare Fig. 9a with Fig. 2; Fig. 9b with Fig. 4d; Fig. 9c with Fig. 12f; and Fig. 9d with Fig. 7g) reveal notable agreement between the products of these two analysis methods. We hence anticipate that the inferences drawn in the following subsections from the behavior of the expansion coefficients a and b are not overly dependent on the SVD methodology adopted here.

c. *Spectra*

The first-order stochastic model as formulated in section 5a is strictly applicable to *local* flux forcing and temperature response on a pointwise basis. In the following discussion, we shall extend this interpretation to the fluctuations in a and b, which actually represent the temporal variability of large-scale spatial *patterns*.

The power spectra of b associated with surface fluxes (hereafter abbreviated as S_F) in the SVDb and SVDc computations are presented in Fig. 10a. The spectra of b for T_o (hereafter abbreviated as S_T) from observations (SVDa) and TOGA-ML output (SVDd) are shown in Fig. 10b. A logarithmic scale is used in both axes of these spectral plots.

It is evident from Fig. 10a that S_F generated in both TOGA and TOGA-ML runs exhibit only a weak dependence on frequency. These results verify the assumption that the atmospheric driving term in Eq. (3) can be approximated as white-noise input to a first-order Markov process. On the other hand, the characteristics of the observed and model-simulated S_T in Fig. 10b are typical of those for red-noise phenomena, with increasing power toward low frequencies. The shape of S_T based on TOGA-ML output bears a notable resemblance to that based on observations. For relatively short periods between 2 and 10 months, both spectra exhibit a uniform slope in the log–log plot shown in Fig. 10b. The values of this slope for the observed and TOGA-ML data, as determined by linear regression (see the bold straight lines superposed on S_T), are

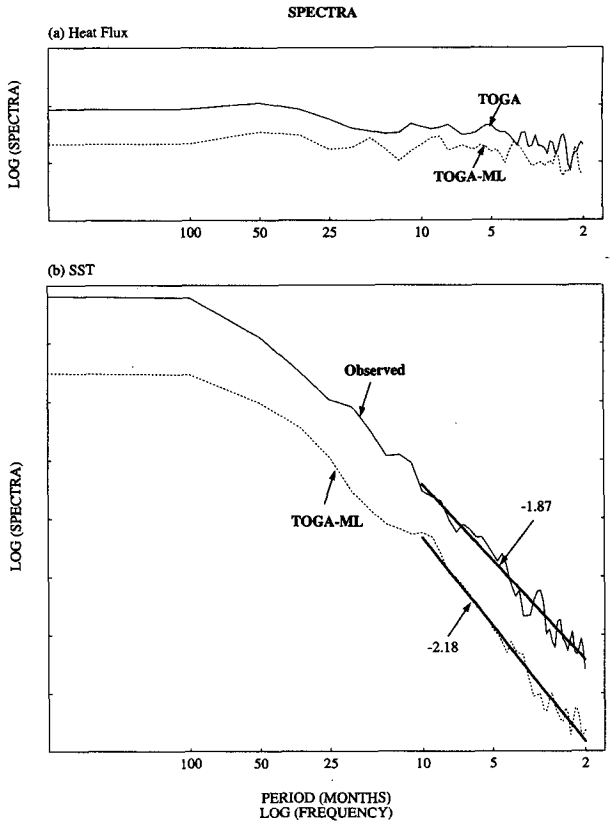

FIG. 10. Log–log plot of the spectra of monthly expansion coefficients b for the right fields in the North Pacific as obtained from (a) SVDb (TOGA-simulated surface fluxes, solid curve) and SVDc (TOGA-ML-simulated surface fluxes, dashed curve) and (b) SVDa (observed SST, solid curve) and SVDd (TOGA-ML-simulated mixed layer temperature, dashed curve). The bold straight lines and numerical values in panel (b) indicate the linear regression slope of the spectra within the period range of 2–10 months. The spectra are computed using the lag correlation method with a maximum lag of 50 months. For the model-generated fields, a power spectrum is first obtained separately for each of the four TOGA or TOGA-ML runs, and the four sets of spectral estimates are then averaged to form the mean spectrum.

-1.87 and -2.18, respectively. These estimates are in good agreement with the -2 slope predicted by Eq. (4) for high frequencies. For very long periods, the observed and simulated S_T level off at a constant value, with no further increase of power toward still lower frequencies. This behavior is again consistent with Eq. (4) for $\omega \ll \lambda$.

The gross characteristics of the spectra for model-simulated fluxes and SST in Fig. 10 are similar to those derived from weather ship data, as presented by Frankignoul and Hasselmann (1977, Fig. 6). Reynolds (1978) has also noted that the power spectrum as given by Eq. (4) provides a good fit of the SST observations over much of the central North Pacific.

The higher power densities in S_F based on TOGA output (solid curve in Fig. 10a) as compared to those

based on TOGA-ML output (dashed curve) are in part due to incorporation in the TOGA-ML experiment of the damping mechanism discussed in section 4a [see Eq. (3)]. The higher power densities in the observed S_T (solid curve in Fig. 10b) as compared to the corresponding result for TOGA-ML (dashed curve) indicate that the amplitude of the SST fluctuations is underestimated in the latter experiment. This finding is consistent with the weaker regression signals based on TOGA-ML data (Fig. 8) relative to the observed data (Fig. 2).

d. Autocorrelation function

As a further test of the applicability of the Markov model for describing air–sea coupling in the North Pacific, the autocorrelation function $R(\tau)$ has been computed using the time series b associated with the SVD patterns of SST based on observed and TOGA-ML data. The distributions of $R(\tau)$ as predicted by Eq. (5) for idealized Markov processes are indicated using thin straight lines in the same figure, with each line corresponding to a different damping coefficient λ.

It is seen that $R(\tau)$ for the TOGA-ML data (dashed curve in Fig. 11) is in reasonable agreement with the functional form of Eq. (5). The damping timescale (λ^{-1}) associated with the model-simulated fluctuations, as deduced from the slopes of the corresponding $R(\tau)$, is 8–10 months. Ignoring effects of atmospheric feedbacks due to changes in V_a, T_a, and q_a (see discussion of experiment B in section 4a), the characteristic λ^{-1} associated with the 50-m mixed layer, as estimated by substituting model climatological data into Eq. (2), is approximately 5 months (see Fig. 6). The longer λ^{-1} of the TOGA-ML output as compared to this estimate suggests that two-way interactions between the mixed layer and the atmosphere, which have been incorporated in TOGA-ML (see right panel of Fig. 5), include processes that counteract the damping mechanism represented in Eq. (2). The possibility of positive feedbacks between the mixed layer and atmosphere in the TOGA-ML scenario is pursued in the next section.

For $\tau < 8$ mo, the distribution of $R(\tau)$ for observational data (solid curve in Fig. 11) is aligned with that of idealized Markov processes with $\lambda^{-1} \sim 10$ mo. For longer τ, the slope of the observed $R(\tau)$ decreases noticeably and corresponds more closely to that of Markov processes with $\lambda^{-1} \sim 16$–18 mo. The longer λ^{-1} of the observed SST variations as compared to the TOGA-ML result may be attributed to a variety of oceanic processes not considered in the model experiment. Moreover, the prescribed mixed layer depth of 50 m in TOGA-ML is probably too shallow, especially during winter. A thicker mixed layer (i.e., larger H) should lengthen λ^{-1}, as Eq. (2) indicates. Frankignoul and Hasselmann (1977, Fig. 7) have also computed $R(\tau)$ using observed SST data and reported that this function exhibits an exponential dependence on τ. Reynolds

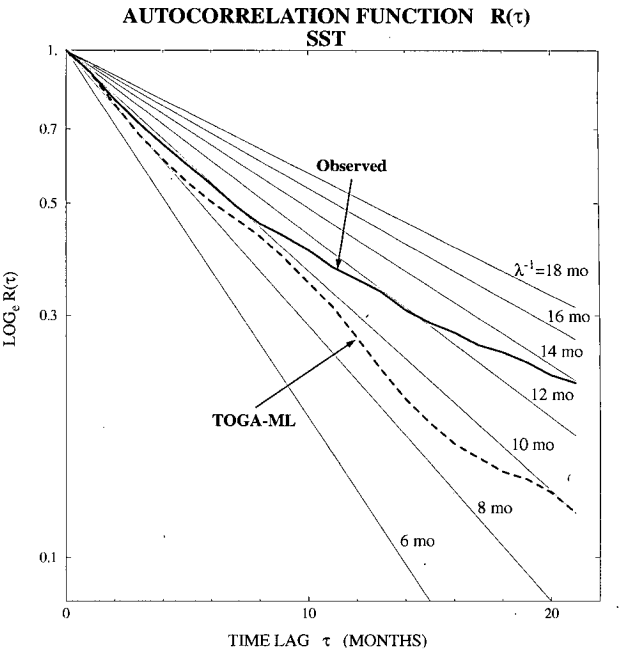

FIG. 11. Plot of the natural logarithm of the autocorrelation function versus time lag, as computed using monthly expansion coefficients b for the right fields in SVDa (observed North Pacific SST: solid curve) and SVDd (TOGA-ML-simulated mixed layer temperature: dashed curve). The thin straight lines denote the autocorrelation function for first-order Markov processes corresponding to various damping timescales λ^{-1} [see Eq. (5)]. To obtain the result for TOGA-ML, the covariance and variance statistics required for the estimation of $R(\tau)$ are evaluated separately from b for each individual 43-yr run, and ensemble averages of these statistics over the four TOGA-ML runs are then taken.

(1978) has estimated λ^{-1} on the basis of SST measurements in the North Pacific. His results yield a mean damping timescale of 0.9 yr.

6. Nature of air–sea coupling in TOGA-ML

a. Regression patterns

As far as the model atmosphere is concerned, the most important distinction between the TOGA and TOGA-ML runs is that the former experiment is subjected to climatological SST conditions at all maritime grid points outside of the tropical Pacific, whereas the latter integration allows for mutual interactions between the atmosphere and an idealized mixed layer at the same grid points (see right panel of Fig. 5). We proceed to evaluate the impact of these interactions on the simulated atmospheric behavior by comparing the output from the TOGA-ML and TOGA experiments.

In Fig. 12 are shown the regression patterns versus the reference TPAC time series of TOGA-ML data for (a) 515-mb height, (b) sea level pressure, (c) temperature, (d) water vapor mixing ratio, and (e) wind speed, and (f) total atmosphere-to-ocean sur-

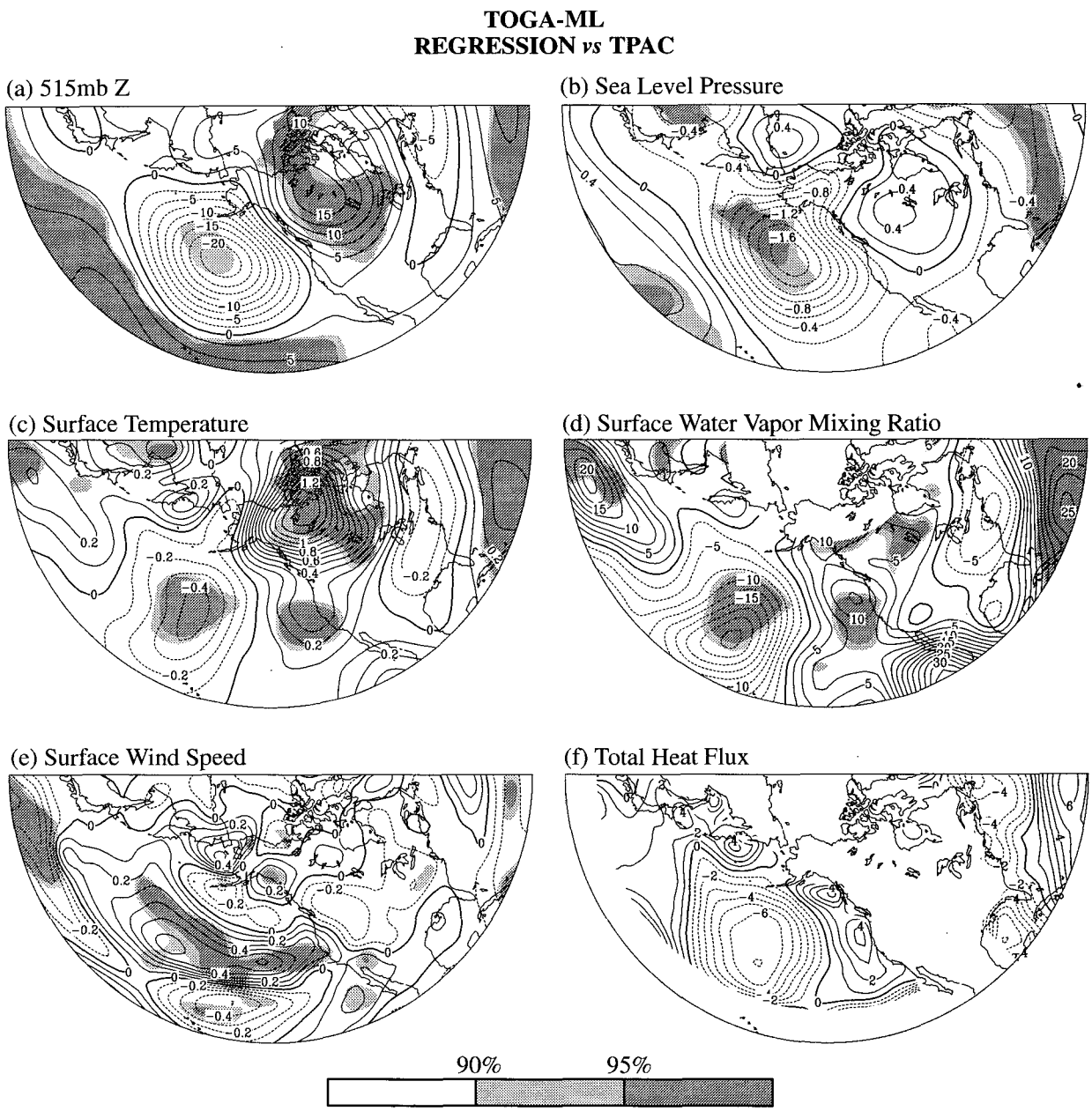

FIG. 12. As in Fig. 3 but based on four-run ensemble averages produced in the TOGA-ML experiment. The variables in panels (a)–(e) are the same as the corresponding panels in Fig. 3. The stippling in these five panels include those grid points where the amplitude of the regression coefficients for TOGA-ML is significantly higher than that for TOGA (see the scale bar at the bottom of the figure for various statistical significance levels exceeded in different sites). Panel (f) shows the regression coefficients for the sum of latent heat, sensible heat, and radiative fluxes in TOGA-ML (contour interval: 1 W m^{-2}).

face flux. Panels (c)–(e) are based on data for the lowest sigma level of the model. Contrasting the patterns in Figs. 3 and 12 reveals that the TOGA-ML charts for the height, pressure, T_a, q_a, and V_a fields bear a strong qualitative resemblance to the corresponding TOGA charts. The regression values in the TOGA-ML results are uniformly larger than those in the TOGA charts by ~30% for the 515-mb height and sea level pressure fields, and by as much as 50%–100% for the T_a, q_a, and V_a fields. Hence the presence of two-way air–sea coupling has the net effect of enhancing the strength of the meteorological anomalies associated with the atmospheric bridge. Manabe and Stouffer (1996) have compared the vari-

ability of T_a simulated in GCM experiments with and without coupling to an oceanic mixed layer. Their results also indicate that two-way air–sea interaction does enhance the variance of T_a.

The statistical significance of the differences between the two sets of regression coefficients in Figs. 3 and 12, as estimated by applying a one-tailed Student's t-test in the manner described in Spiegel (1961) and making the crude assumption that the sample has 42 − 2 = 40 degrees of freedom, is indicated in the respective panels of Fig. 12 by stippling. This statistical testing is performed only over those grid points that satisfy *both* of the following criteria: 1) the local regression values based on TOGA-ML and TOGA data must share the same polarity and 2) the absolute value of the regression coefficient for TOGA-ML must be larger than that of the TOGA result. It is seen that the near-surface atmospheric pressure, temperature, humidity, and wind anomalies associated with the deeper low pressure center in the central North Pacific in the TOGA-ML experiment are significantly more intense than those in TOGA, at a confidence level exceeding ~95%.

The amplitude of the regression pattern for total surface flux based on TOGA-ML (Fig. 12f) is lower than that based on TOGA (Fig. 4d). This finding is consistent with the generally lower power in the spectrum of the SVD expansion coefficients for surface fluxes in TOGA-ML as compared to the corresponding result for TOGA (Fig. 10a). The difference between the surface fluxes in TOGA and TOGA-ML is the net result of two opposing processes incorporated in the latter experiment: the feedback of T_o' on the fluxes [which weakens air–sea exchange, see discussion related to Eq. (3)] and enhancement of the near-surface atmospheric anomalies (which strengthens the atmospheric driving and hence the surface fluxes). The reduced surface flux amplitude simulated in the TOGA-ML signifies that the damping effect due to T_o fluctuations is relatively more important.

b. Persistence characteristics

We now turn our attention to those aspects of the *day to day* atmospheric fluctuations that contribute to amplitude enhancements of the *seasonal mean* anomalies appearing in the TOGA-ML runs. In order to develop suitable temporal indexes depicting the high-frequency atmospheric changes, a principal component (PC) analysis is performed on the daily data for 515-mb height in various model runs. The climatological seasonal cycle is removed by subtracting the 5-day running mean of the long-term average of each calendar day from the daily time series for individual years. The detrended data are further processed through a 21-point low-pass digital filter analogous to that used by Blackmon and Lau (1980) so as to retain fluctuations with timescales of 5 days and longer. The domain for the PC analysis extends eastward from 130°E to 50°W.

The same PC analysis has been applied separately to the output from TOGA-ML and TOGA, as well as to three other experiments described elsewhere: GOGA (in which observed monthly SST fluctuations are prescribed in the near-global ocean domain, see LN94), MOGA (in which the monthly varying SST forcing is prescribed in the midlatitude North Pacific only, see LN94), and a 100-yr control experiment subjected to climatological SST conditions throughout the World Ocean, with no interannual variation in the oceanic forcing anywhere (see Ting and Lau 1993). These five individual experiments yield essentially the same set of spatial patterns for the first several PC modes. The pattern associated with the second PC mode for the TOGA-ML experiment is presented in Fig. 13. This particular mode is selected for further diagnosis by virtue of its resemblance to the regression pattern accompanying ENSO events in the tropical Pacific (compare Fig. 13 with Figs. 12a and 3a). The patterns of the second PC mode for the other four experiments (not shown) are almost identical to Fig. 13. The fraction of domain-integrated variance explained by the second PC mode is 11.8%, 12.2%, 12.1%, 12.9%, and 12.1% for the TOGA-ML, TOGA, GOGA, MOGA, and control experiments, respectively. The first PC mode (not shown), which explains slightly more variance (14.6% in the TOGA-ML run), is characterized by a primary center over Alaska and bears little resemblance to the patterns in Figs. 12a and 3a.

The expansion coefficients (hereafter referred to as c) for a given PC mode depict the temporal evolution of the amplitude and polarity of height anomaly patterns with a spatial structure similar to that mode. The time series of c associated with the second PC mode for the TOGA-ML and TOGA experiments is shown in Fig. 14 for the 1982/83 winter (which corresponds to the most prominent warm ENSO event in the period considered here, see Fig. 1a) and for all four individual runs in each experiment. These sample time series suggest that fluctuations in c in the TOGA-ML runs tend to maintain a given polarity for longer durations than the corresponding TOGA variations. The strengthening of the seasonally averaged anomalies in the presence of midlatitude air–sea coupling, as noted earlier in the comparison between regression maps of seasonal means for TOGA-ML and TOGA, is hence related to the enhanced temporal persistence in the day to day evolution of a principal mode of variability in TOGA-ML. The role of extratropical air–sea interactions in maintaining a more persistent cold SST anomaly in the central North Pacific has also been identified in the recent model runs of Gallimore (1995).

Another striking feature of the time series displayed in Fig. 14 is the large variability among the four individual sample runs for a given experiment (TOGA-ML or TOGA). The considerable scatter among different realizations of the model response to a given SST forc-

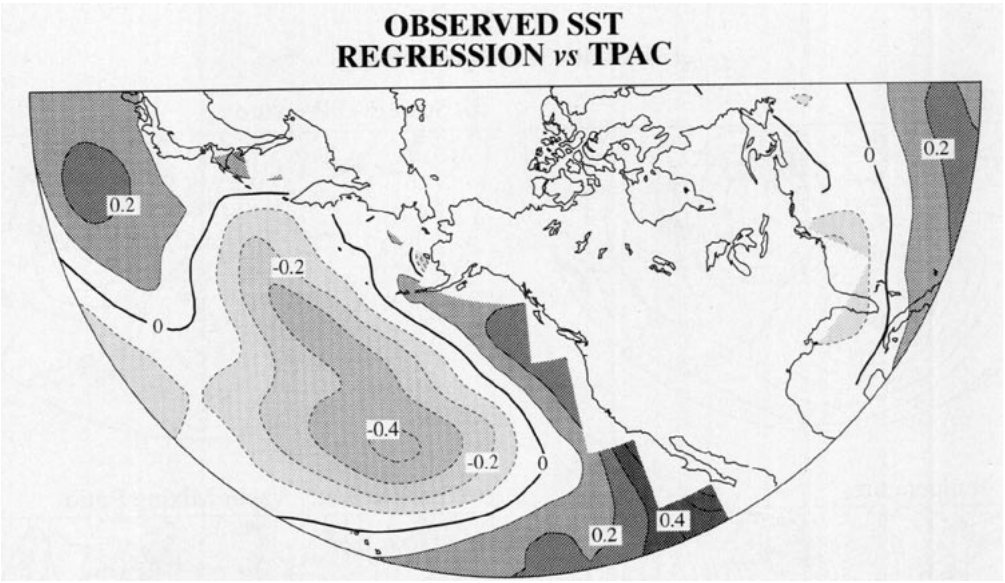

FIG. 13. Spatial pattern of the second principal component of the low-pass filtered wintertime daily 515-mb height field simulated in the TOGA-ML experiment, as constructed by mapping the distribution of the temporal correlation coefficients of the daily 515-mb height values at individual grid points versus the time series of temporal coefficients associated with the second principal component. Contour interval: 1×10^{-1}. The input data for the PC analysis consist of unnormalized daily values for all winters and all four individual realizations of the TOGA-ML experiment. The winter season is defined as the 131-day period from 11 November to 21 March.

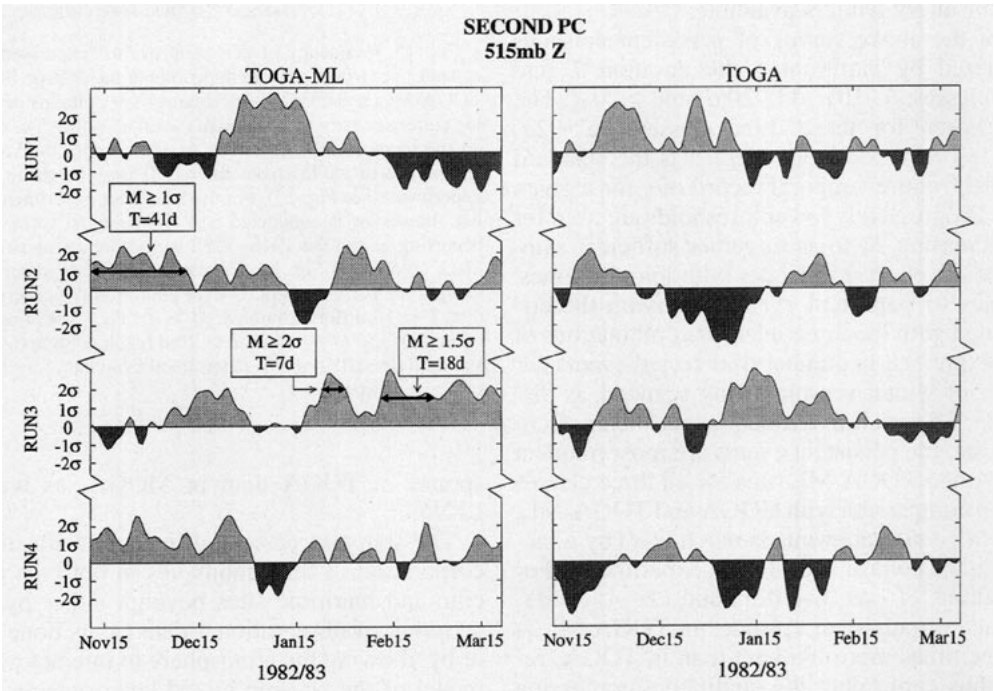

FIG. 14. Time series of temporal coefficients c associated with the second principal component of the low pass filtered wintertime daily 515-mb height simulated in the four individual runs of the TOGA-ML (left panel) and TOGA (right panel) experiments during the warm ENSO winter of 1982/83. All values of c are expressed in units of standard deviation σ as determined from data for the entire length of a given experiment. Examples of several persistent episodes satisfying various amplitude/duration criteria are given in the left panel.

ing is also evident in the runs analyzed in LN94 (see their Fig. 7).

The above qualitative inferences on persistence behavior of the model atmosphere are drawn from the simulation during a single winter by two specific experiments. We proceed to broaden the scope of this investigation by conducting a more quantitative and objective survey of the persistence characteristics in all five available model scenarios and in a larger set of winters. The frequency of occurrence of persistent events in a given experiment is obtained by scanning the time series of c for the second PC mode of 515-mb height for selected winters in all individual model runs available for that experiment. Following a procedure analogous to that used by Dole and Gordon (1983), each persistent event is characterized by two attributes: the duration of the event T and the (preset) threshold value M that c for each consecutive day in this event must exceed. Examples of several persistent events satisfying various (M, T) criteria are illustrated in Fig. 14. The number of persistent events in various (M, T) categories is determined separately for the TOGA-ML, TOGA, GOGA, MOGA, and control experiments. With the exception of the control run, the analysis is applied to the set of eight major warm ENSO events occurring in the 1946–1988 period (i.e., the winters beginning with the Decembers of 1957, 1965, 1969, 1972, 1976, 1982, 1986, and 1987, see black columns in Fig. 1a). For the control experiment, the scanning is performed for all 99 winters available.

Results of the above survey of persistent episodes are summarized by partitioning the duration T into three broad classes: 6–10 d, 11–20 d, and >20 d. The M values chosen for these three classes are $+2\sigma$, $+1.5\sigma$, and $+1\sigma$, respectively. Here σ is the standard deviation of the entire temporal record of c for a given experiment. Progressively lower thresholds are used for events of increasing T, so as to gather sufficient samples of the relatively rare episodes with long lifetimes. The frequency of persistent events satisfying the criteria associated with the three selected combinations of (M, T), as expressed in number of detected events per total number of winter seasons being scanned, is displayed in Fig. 15 for all five model experiments. Generally speaking, the persistent events are most frequent in the GOGA and TOGA-ML runs for all three classes of (M, T). In comparison with GOGA and TOGA-ML, the number of persistent events is much less (by a factor of 2–4) in the control and MOGA experiments. For the combinations of $(2\sigma$, 6–10 d) and $(1\sigma$, >20 d), the occurrence of persistent episodes in TOGA-ML is two and three times more frequent than in TOGA, respectively, thus confirming the qualitative impression gained from inspection of Fig. 14. For the combinations of $(2\sigma$, 6–10 d) and $(1.5\sigma$, 11–20 d), the number of events simulated in TOGA is more than twice that appearing in MOGA. This result is consistent with the much stronger seasonally averaged atmospheric response in TOGA than in MOGA, as was noted in LN94.

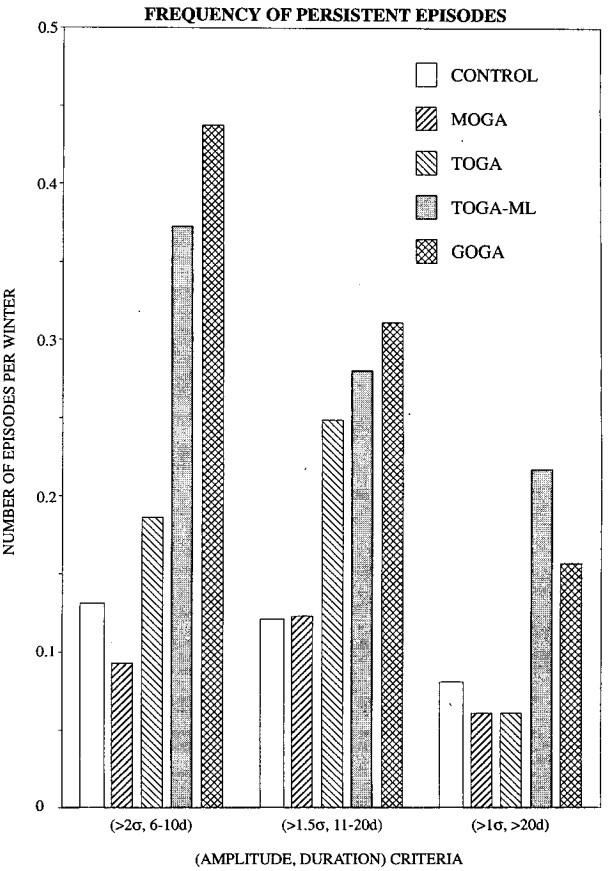

FIG. 15. Frequency of persistent events (expressed in number of episodes per winter season) appearing in the control, MOGA, TOGA, TOGA-ML, and GOGA experiments (see columns of various hatching pattern density and legend in the upper right). The census is based on the temporal coefficients c associated with the second principal component of the low-pass filtered 515-mb height in the respective experiment (see Fig. 13). For the latter four experiments in the above list, the survey is conducted only on the eight warm ENSO winters occurring within the 1946–1988 period (i.e., winters highlighted by black columns in Fig. 1a). Persistent events are identified separately using three pairs of amplitude (M)/duration (T) criteria: $M \geq +2\ \sigma$, $6 \leq T \leq 10$ d (left columns); $M \geq +1.5\sigma$, $11 \leq T \leq 20$ d (middle columns); and $M \geq +1\ \sigma$, $T > 20$ d (right columns), where σ is the standard deviation of c as determined from data for the entire length of a given experiment.

The statistics presented in Fig. 15 illustrate that incorporation of SST anomalies in both the tropical Pacific and maritime sites beyond, either by direct prescription of observational data (as is done in GOGA) or by allowing the atmosphere to interact with a simple model of the oceanic mixed layer outside the tropical Pacific (as is done in TOGA-ML), leads to a higher degree of atmospheric persistence when compared to the simulation with SST forcing in the tropical Pacific only (TOGA). The comparable frequency of events in the MOGA and control runs in all classes of T indicates

that the persistence behavior of the model atmosphere is not significantly altered by insertion of SST anomalies in the midlatitude North Pacific alone. The appearance of the second PC mode (Fig. 13) in MOGA may hence be attributed mostly to internal atmospheric variability, with extratropical SST forcing playing a negligible role.

7. Conclusions and discussion

The present study complements the works of several earlier investigators and LN94 on the atmospheric bridge linking SST anomalies in the tropical Pacific with those in the midlatitude oceans. A more thorough documentation is offered on the atmospheric circulation patterns and atmosphere–ocean energy exchange associated with this mechanism (Figs. 3 and 4). The effects of the atmospheric response to ENSO on the midlatitude North Pacific and western North Atlantic are tested directly by conducting a suite of experiments with increasing degree of interaction between the atmosphere and a simple mixed layer model of the ocean (Fig. 5). It is demonstrated that this idealized mixed layer, when driven by surface fluxes generated in the TOGA run and modulated by a linear damping process, captures the essential temporal and spatial behavior of SST variations observed in the northern oceans (Fig. 7). The analogy between the first-order Markov process and the simple system relating mixed layer temperature tendency to surface flux forcing and damping is then critically examined. The predominantly white spectrum of the input data for surface fluxes (Fig. 10a), and red spectrum of the temperature response (Fig. 10b), as well as the exponential form of the lagged autocorrelation function of the temperature output (Fig. 11), confirms that the first-order stochastic process with a characteristic damping timescale is a relevant conceptual framework for viewing midlatitude air–sea interaction.

Comparison between the simulations in the TOGA and TOGA-ML runs (Figs. 3 and 12) indicates that incorporation of two-way air–sea coupling in the latter experiment significantly enhances the amplitude of the near-surface atmospheric anomalies. Such intensification of the seasonally averaged atmospheric circulation is then traced to the more frequent appearance of persistent anomalous episodes in the TOGA-ML experiment (Figs. 14). A survey of persistence characteristics of the model output from five different model scenarios (Fig. 15) offers a broad perspective on the impact of SST anomalies in different regions on low-frequency atmospheric behavior. This analysis indicates that the ranking of the maritime sites, in order of decreasing influence on extratropical atmospheric variability, appears to be as follows: tropical Pacific in combination with other sites in the World Ocean (GOGA and TOGA-ML), tropical Pacific only (TOGA), and midlatitude ocean only (MOGA).

It is noteworthy that, despite the deterministic prescription of observed tropical Pacific SST episodes in the TOGA and TOGA-ML experiments, the spectra of the simulated extratropical heat flux forcing related to ENSO remain essentially white (see Fig. 10a), with power densities at ENSO timescales (i.e., 2 yr and longer) being only slightly higher than those associated with month to month fluctuations. The latter, short-term variability is primarily a manifestation of internal dynamical processes operating within the midlatitude atmosphere. These "background" fluctuations exist regardless of the presence or absence of any tropical SST forcing. By coupling a model atmosphere with a mixed layer similar to that used in this study, Gallimore (1995) and Delworth (1996) have discerned well-defined modes of air–sea coupling in the North Pacific and North Atlantic, respectively, even when no SST anomaly is prescribed anywhere in the World Ocean. Signals related to the ENSO forcing and the atmospheric bridge mechanism would hence have to compete with the considerable level of variability associated with random, internally generated atmospheric disturbances. It is also important to bear in mind that the midlatitude atmospheric response to ENSO forcing is known to be strongest in the winter season (e.g., see Chen 1982). As a result, spectra based on time series for all months of the year are not particularly effective in revealing the impact of ENSO on extratropical atmospheric variability. On the other hand, diagnostic techniques that focus on the spatial pattern of the wintertime atmospheric circulation (e.g., see the regression charts in Figs. 3, 4, and 12) and temporal persistence statistics of carefully selected wintertime events (e.g., see Fig. 15) are more successful in delineating the midlatitude effects of ENSO.

This study is devoted to the understanding of the relationship between SST changes in the tropical Pacific and those in the extratropical oceans in the Northern Hemisphere. Equally striking in the global SST anomaly chart during ENSO events (e.g., see Fig. 3b of LN94) is the positive correlation between temperatures in the tropical Pacific and Indian Oceans. The latter connection may be partially attributed to the east–west movements of the rainbelt in the tropical Indian Ocean and the western Pacific during ENSO episodes. The attendant shifts in the distribution of cloud cover would lead to changes in the amount of incident solar radiation at the ocean surface, thereby altering the local SST (see LN94). Other possible contributing factors to the link between the tropical Pacific and Indian Oceans are the changes in equatorwide tropospheric temperature (Yulaeva and Wallace 1994) and near-surface atmospheric circulation (LN94). These temperature and wind anomalies could in turn affect the SST over the Indian Ocean.

The mixed layer temperature simulated by the TOGA-ML experiment in the tropical Indian Ocean (not shown) is indeed positively correlated with the

prescribed SST forcing in the tropical central Pacific, although the amplitude of these model-generated anomalies is noticeably weaker than the observed values. This preliminary finding supports the notion that atmospheric processes do play a role in linking the oceanic variability in different tropical basins. However, more investigations remain to be made to improve our understanding of the nature of the atmospheric bridge spanning the tropical Pacific and Indian Oceans, as well as the relationships (if any) among the tropical Pacific, tropical Atlantic, and the southern oceans. The available ship and satellite measurements in the tropical oceans (e.g., Liu and Gautier 1990) need to be scrutinized for coherent signals in various forms of energy exchange during ENSO events. Additional model experimentation (e.g., TOGA-ML runs with and without cloud–radiation feedbacks and simulations with more realistic ocean dynamics) and diagnosis need to be performed to identify the mechanisms contributing to the covariability among different tropical maritime sites.

The stronger atmospheric signal in the North Pacific/North American sector in TOGA-ML as compared to that in TOGA (see discussion in section 6a) could result from the incremental forcing associated with the mixed layer temperature anomalies in the Indian Ocean generated in TOGA-ML. Observational studies (e.g., Kawamura 1994) have presented evidence on the link between SST variations in the Indian Ocean and the Pacific/North American pattern. Further analysis is required to assess the relative roles of in situ air–sea interaction in the extratropics and remote SST forcing originating from the Indian Ocean in amplifying the midlatitude atmospheric response.

Since the mixed layer examined in this study is motionless and has a constant, spatially uniform depth, the model atmosphere and ocean can influence each other only through the heat fluxes across the interface between the two media. The virtue of the highly simplified mixed layer used here lies in the ease with which it can be incorporated into various model experiments and the straightforward manner in which the model output can be interpreted. Experiments by Alexander (1992a) using mixed layers with more complete ocean physics confirm that surface energy exchange is the most important coupling mechanism for the problem at hand. Nonetheless, it would still be of interest to ascertain the contributions to midlatitude air–sea interaction by other mixed layer processes such as Ekman pumping, vertical displacement of the thermocline, advection by surface ocean currents, and entrainment of deep ocean water. Those processes in which the seasonal cycle or the deep ocean are active participants could modify the nature of air–sea feedbacks associated with the atmospheric bridge on multiyear timescales and thereby exert considerable influences on the low-frequency variability of the coupled system in the extratropics.

In the present study, the correlation/regression analysis of the linkages between the TPAC time series (see Fig. 1a) and ocean–atmosphere fluctuations in the extratropics has been performed using unfiltered winter averages for individual years. Hence a large variety of fluctuations with timescales ranging from interannual (such as the individual ENSO cycles) to interdecadal (such as the prolonged warm episode in TPAC during 1976–1988) periods could conceivably contribute to the statistics presented here. Deser and Blackmon (1995) have identified an interannual mode of observed SST variability in the North Pacific (similar to Fig. 2) that is linked to ENSO, as well as an interdecadal mode that is independent of ENSO. In view of this notable timescale dependence of the connection between SST anomaly patterns in the tropical and North Pacific, a more detailed diagnosis of the model output (e.g., by applying temporal filters) could yield fresh insights in the differences and similarities between modes of tropical–extratropical interactions in various frequency regimes.

Acknowledgments. We would like to thank Drs. M. A. Alexander, D. S. Battisti, I. M. Held, and J. M. Wallace for helpful discussions on various aspects of this study. The comments by the above colleagues and by Drs. J. L. Anderson, T. L. Delworth, J. R. Lanzante, P.-T. Peng, and the official reviewers were very helpful in clarifying some of the discussion in the manuscript. This work has benefited from the participation of NCL as a member of the Advisory Committee of the NOAA Equatorial Pacific Ocean Climate Studies (EPOCS) Program, for which Dr. Stan P. Hayes had served with distinction as chairperson. This investigation has been conducted in association with a NOAA/Universities collaborative effort aimed at understanding atmospheric variability associated with boundary forcings and the maintenance of regional climates. Support of this long-term effort by the NOAA Climate and Global Change Program is gratefully acknowledged.

REFERENCES

Alexander, M. A., 1990: Simulation of the response of the North Pacific Ocean to the anomalous atmospheric circulation associated with El Niño. *Climate Dyn.*, **5**, 53–65.

——, 1992a: Midlatitude atmosphere–ocean interaction during El Niño. Part I: The North Pacific Ocean. *J. Climate*, **5**, 944–958.

——, 1992b: Midlatitude atmosphere–ocean interaction during El Niño. Part II: The Northern Hemisphere atmosphere. *J. Climate*, **5**, 959–972.

Blackmon, M. L., and N.-C. Lau, 1980: Regional characteristics of the Northern Hemisphere wintertime circulation: A comparison of the simulation of a GFDL general circulation model with observations. *J. Atmos. Sci.*, **37**, 497–514.

Bretherton, C. S., C. Smith, and J. M. Wallace, 1992: An intercomparison of methods for finding coupled patterns in climate data. *J. Climate*, **5**, 541–560.

Cayan, D. R., 1992a: Latent and sensible heat flux anomalies over the northern oceans: The connection to monthly atmospheric circulation. *J. Climate*, **5**, 354–369.

——, 1992b: Latent and sensible heat flux anomalies over the northern oceans: Driving the sea surface temperature. *J. Phys. Oceanogr.,* **22,** 859–881.

Chen, W. Y., 1982: Fluctuations in Northern Hemisphere 700-mb height field associated with the Southern Oscillation. *Mon. Wea. Rev.,* **110,** 808–823.

Delworth, T. L., 1996: North Atlantic interannual variability in a coupled ocean–atmosphere model. *J. Climate,* in press.

——, and S. Manabe, 1988: The influence of potential evaporation on the variabilities of simulated soil wetness and climate. *J. Climate,* **1,** 523–547.

Deser, C., and M. L. Blackmon, 1995: On the relationship between tropical and North Pacific sea surface temperature variations. *J. Climate,* **8,** 1677–1680.

Dole, R. M., and N. D. Gordon, 1983: Persistent anomalies of the extratropical Northern Hemisphere wintertime circulation: Geographical distribution and regional persistence characteristics. *Mon. Wea. Rev.,* **111,** 1567–1586.

Ferranti, L., F. Molteni, and T. N. Palmer, 1994: Impact of localized tropical and extratropical SST anomalies in ensembles of seasonal GCM integrations. *Quart. J. Roy. Meteor. Soc.,* **120,** 1613–1645.

Frankignoul, C., and K. Hasselmann, 1977: Stochastic climate models, Part II: Application to sea-surface temperature anomalies and thermocline variability. *Tellus,* **29,** 289–305.

——, and R. W. Reynolds, 1983: Testing a dynamical model for midlatitude sea surface temperature anomalies. *J. Phys. Oceanogr.,* **13,** 1131–1145.

Gallimore, R. G., 1995: Simulated ocean-atmosphere interaction in the North Pacific from a GCM coupled to a constant-depth mixed layer. *J. Climate,* **8,** 1721–1737.

Gordon, C. T., and W. F. Stern, 1982: A description of the GFDL global spectral model. *Mon. Wea. Rev.,* **110,** 625–644.

Graham, N. E., T. P. Barnett, R. Wilde, U. Schlese, and L. Bengtsson, 1994: On the roles of tropical and midlatitude SSTs in forcing interannual to interdecadal variability in the winter Northern Hemisphere circulation. *J. Climate,* **7,** 1416–1441.

Hasselmann, K., 1976: Stochastic climate models. *Tellus,* **28,** 473–484.

Hsiung, J., and R. E. Newell, 1983: The principal nonseasonal modes of variation of global sea surface temperature. *J. Phys. Oceanogr.,* **13,** 1957–1967.

Kawamura, R., 1994: A rotated EOF analysis of global sea surface temperature variability with interannual and interdecadal scale. *J. Phys. Oceanogr.,* **24,** 707–715.

Lau, N.-C., and M. J. Nath, 1994: A modeling study of the relative roles of tropical and extratropical SST anomalies in the variability of the global atmosphere–ocean system. *J. Climate,* **7,** 1184–1207.

Lemke, P., E. W. Trinkl, and K. Hasselmann, 1980: Stochastic dynamic analysis of polar sea ice variability. *J. Phys. Oceanogr.,* **10,** 2100–2120.

Liu, W. T., and C. Gautier, 1990: Thermal forcing on the tropical Pacific from satellite data. *J. Geophys. Res.,* **95**(C8), 13 209–13 217, 13 579–13 580.

Luksch, U., and H. von Storch, 1992: Modeling the low-frequency sea surface temperature variability in the North Pacific. *J. Climate,* **5,** 893–906.

Manabe, S., and R. J. Stouffer, 1988: Two stable equilibria of a coupled ocean–atmosphere model. *J. Climate,* **1,** 841–866.

——, and ——, 1996: Low-frequency variability of surface air temperature in a 1000-year integration of a coupled ocean–atmosphere model. *J. Climate,* **9,** 376–393.

Miller, A. J., D. R. Cayan, T. P. Barnett, N. E. Graham, and J. M. Oberhuber, 1994: Interdecadal variability of the Pacific Ocean: Model response to observed heat flux and wind stress anomalies. *Climate Dyn.,* **9,** 287–302.

Pan, Y. H., and A. H. Oort, 1990: Correlation analyses between sea surface temperature anomalies in the eastern equatorial Pacific and the World Ocean. *Climate Dyn.,* **4,** 191–205.

Rasmusson, E. M., and T. H. Carpenter, 1982: Variations in tropical sea surface temperature and surface wind fields associated with the Southern Oscillation–El Niño. *Mon. Wea. Rev.,* **110,** 354–384.

Reynolds, R. W., 1978: Sea surface temperature anomalies in the North Pacific Ocean. *Tellus,* **30,** 97–103.

Spiegel, M. R., 1961: *Theory and Problems of Statistics.* Schaum's Outline Series. Schaum Publishing, 359 pp.

Ting, M., and N.-C. Lau, 1993: A diagnostic and modeling study of the monthly mean wintertime anomalies appearing in a 100-yr GCM experiment. *J. Atmos. Sci.,* **50,** 2845–2867.

Wallace, J. M., C. Smith, and C. S. Bretherton, 1992: Singular value decomposition of wintertime sea surface temperature and 500-mb height anomalies. *J. Climate,* **5,** 561–576.

Weare, B. C., A. Navato, and R. E. Newell, 1976: Empirical orthogonal analysis of Pacific Ocean sea surface temperatures. *J. Phys. Oceanogr.,* **6,** 671–678.

Woodruff, S. D., R. J. Slutz, R. L. Jenne, and P. M. Steurer, 1987: A Comprehensive Ocean–Atmosphere Data Set. *Bull. Amer. Meteor. Soc.,* **68,** 1239–1250.

Yulaeva, E., and J. M. Wallace, 1994: The signature of ENSO in global temperature and precipitation fields derived from the Microwave Sounding Unit. *J. Climate,* **7,** 1719–1736.